Limits on intrinsic charm production from the SeaQuest experiment

R. Vogt ⬤

Nuclear and Chemical Sciences Division, Lawrence Livermore National Laboratory, Livermore, California 94551, USA
and Department of Physics and Astronomy, University of California, Davis, California 95616, USA

Background: A nonperturbative charm production contribution, known as intrinsic charm, has long been speculated but has never been satisfactorily proven. The SeaQuest experiment at the Fermi National Accelerator Laboratory (FNAL) is in an ideal kinematic region to provide evidence of J/ψ production by intrinsic charm.
Purpose: J/ψ production in the SeaQuest kinematics is calculated with a combination of perturbative quantum chromodynamics (QCD) and intrinsic charm to see whether the SeaQuest data can put limits on an intrinsic charm contribution.
Methods: J/ψ production in perturbative QCD is calculated to next-to-leading order in the cross section. Cold nuclear matter effects include nuclear modification of the parton densities, absorption by nucleons, and p_T broadening by multiple scattering. The J/ψ contribution from intrinsic charm is calculated assuming production from a $|uudc\bar{c}\rangle$ Fock state.
Results: The nuclear modification factor R_{pA} is calculated as a function of x_F and p_T for $p + \mathrm{C}$, $p + \mathrm{Fe}$, and $p + \mathrm{W}$ interactions relative to $p + \mathrm{d}$. Previous data from the E866 experiment at FNAL is also shown and compared with the calculations.
Conclusions: The SeaQuest kinematic acceptance is ideal for testing the limits on intrinsic charm in the proton.

I. INTRODUCTION

Production of J/ψ has long been studied in a variety of environments, from more elementary collisions such as $p + p$ and $p + \bar{p}$, to protons on nuclei, $p + A$, and in nucleus-nucleus collisions, $A + A$. While many of the earlier studies of J/ψ production in $p + A$ collisions were made in fixed-target configurations [1–8], more recently production has predominantly been studied at hadron and nuclear colliders, in particular at the Relativistic Heavy-Ion Collider (RHIC) at Brookhaven [9,10] and the Large Hadron Collider (LHC) at CERN [11–14]. However, in the last several years, J/ψ production has been studied by the SeaQuest experiment at Fermilab [15] in a fixed-target setup and at a lower incident-proton energy than previous experiments, allowing unprecedented forward coverage probing partons carrying a large fraction x_1 of the incident-proton momentum.

This large x_1 coverage is of interest because it is ideal for setting limits on any $c\bar{c}$ component of the proton wave function, proposed by Brodsky and collaborators [16–18]. There have been some tantalizing hints [1,19,20] but no concrete confirmation so far. Fixed-target data usually do not cover the far forward x_F region or have done so with insufficient statistics to make any definitive statement. Production at collider energies is ineffective for such studies because the collider kinematics put large x partons from the projectiles outside the detector coverage [21]. Several additional new fixed-target experiments have been proposed [22,23] or have taken data [24], including using the LHC for fixed-target studies [23,24], but all are higher energy than SeaQuest.

Earlier studies of J/ψ production at fixed-target experiments parametrized the nuclear dependence of J/ψ production as a power law [1–8],

$$\sigma_{pA} = \sigma_{pN} A^{\alpha}, \qquad (1)$$

where A is the target mass and σ_{pA} and σ_{pN} are the production cross sections in proton-nucleus and proton-nucleon interactions, respectively. If J/ψ production is unaffected by the presence of the nucleus, σ_{pA} would grow linearly with A and $\alpha = 1$. However, a less than linear A dependence has been observed [1–8]. Typical values of α were between 0.9 and 1. This A dependence was previously used to determine an effective nuclear absorption cross section [5,25,26] under the assumption that the deviation of α from unity was solely due to J/ψ dissociation by nucleons. However, more detailed studies of α as a function of the longitudinal momentum fraction x_F and transverse momentum p_T revealed a more complex picture. Indeed, it has long been known that α decreases as a function of x_F [1–3,8] and increases with p_T [3,6,8], neither of which can be accounted for by nuclear absorption alone. A number of cold nuclear matter effects can contribute to this dependence. These include nuclear modifications of the

parton distributions in nucleons in a nucleus relative to those of a free proton [27], and energy loss or transverse momentum broadening due to multiple scattering as the projectile transits the nucleus [28–30], in addition to absorption. It has however, proven difficult for most model calculations to describe J/ψ production on nuclear targets as a function of x_F and p_T with these cold nuclear matter effects alone.

The NA3 Collaboration [1] proposed dividing J/ψ production into two components that they referred to as hard and diffractive for the nuclear volume-like and surface-like dependencies, respectively,

$$\frac{d\sigma_{pA}}{dx_F} = A^{\alpha'} \frac{d\sigma_h}{dx_F} + A^{\beta} \frac{d\sigma_d}{dx_F}. \qquad (2)$$

The hard component is the perturbative QCD contribution discussed so far while the so-called diffractive component has been attributed to intrinsic charm, $c\bar{c}$ pairs in the proton wave function [16–18]. Since the charm quark mass is large, these intrinsic heavy quark pairs carry a significant fraction of the longitudinal momentum and contribute at large x_F whereas perturbative charm production decreases strongly with x_F. The light spectator quarks in the intrinsic $c\bar{c}$ state interact on the nuclear surface, leading to an approximate $A^{2/3}$ dependence [18]. The NA3 Collaboration found $\alpha' = 0.97$ and $\beta = 0.71$ for proton projectiles [1]. This value of β is approximately consistent with a nuclear dependence due to surface interactions relative to interactions with the nuclear volume, as in hard scattering [18]. Such an approach was employed to compare with the NA3 measurements [31] for incident protons at 200 GeV and other fixed-target experiments at higher energies [32].

The SeaQuest experiment at FNAL, with a 120 GeV incident proton beam, is in an ideal kinematic regime to test intrinsic charm production. Its J/ψ acceptance is in the region $0.4 < x_F < 0.95$ and $p_T < 2.3$ GeV. They have measured the x_F and p_T dependence of J/ψ production in $p + p$, $p + \mathrm{d}$, $p + \mathrm{C}$, $p + \mathrm{Fe}$ and $p + \mathrm{W}$ interactions [33]. A similar two-component model is employed to make predictions for these measurements, at energies and with kinematic acceptance favorable to intrinsic charm, in this work. The results are expressed through the nuclear modification, R_{pA}, factor, the ratio of the per nucleon cross section in $p + A$ collisions relative to $p + \mathrm{d}$ interactions at the same energy, instead of α, as previously employed.

Previous measurements at FNAL were also made with an 800 GeV incident proton beam on several nuclear targets [3,4,6] measured α as a function of x_F and p_T. The last of these, E866, reported α over the full x_F range, $-0.1 \leqslant x_F \leqslant 0.93$, and as a function of p_T in three x_F bins: $-0.1 \leqslant x_F \leqslant 0, 3$ (low x_F); $0.2 \leqslant x_F \leqslant 0.6$ (intermediate x_F); and $0.3 \leqslant x_F \leqslant 0.93$ (high x_F). Data were taken in $p + p$, $p + \mathrm{Be}$, $p + \mathrm{Fe}$, and $p + \mathrm{W}$ interactions. Characterizing the data from all three nuclear targets into a single α rather than a nuclear modification factor for each target reduces the potential information. Nonetheless, the range of these data can provide a point of comparison for the SeaQuest calculations shown here. Calculations of $\alpha(x_F)$ were made with an earlier version of a similar model [32]. However, the perturbative QCD calculations were at leading order, with no calculation of the

p_T dependence. The modifications of the parton densities in nuclei used in the previous work have now been supplanted by newer evaluations. In addition, in that work, initial-state energy loss was considered while here p_T broadening is included instead.

The calculation of J/ψ production in perturbative QCD is presented in Sec. II. The cold nuclear matter effects included in the calculation are also introduced. The x_F and p_T distributions from intrinsic charm are presented in Sec. III, along with a discussion of the nuclear dependence. Section IV presents the results for the modification of J/ψ production in nuclear targets at SeaQuest, both for perturbative QCD effects alone and including the intrinsic charm contribution. Comparison is also made to the data from the E866 experiment in Sec. IV. The conclusions are presented in Sec. V.

II. J/ψ PRODUCTION AND COLD NUCLEAR MATTER EFFECTS IN PERTURBATIVE QUANTUM CHROMODYNAMICS

This section describes J/ψ production in perturbative QCD and describes how cold nuclear matter effects are implemented in this work.

The J/ψ production mechanism remains an unsettled question, with a number of approaches having been introduced [34–36]. In the calculations presented here, the color evaporation model (CEM) [34] is employed. This model, together with the improved color evaporation model [36], can describe the x_F and p_T distributions of J/ψ production, including at low p_T where other approaches have some difficulties and may require a p_T cut [37]. The CEM calculations are described in Sec. II A. The remainder of this section discusses nuclear modifications of the parton densities, nPDF effects, Sec. II B; absorption by nucleons, Sec. II C; and transverse momentum broadening, Sec. II D; are implemented in this work.

A. Charmonium production in the color evaporation model

The CEM [34] is employed to calculate J/ψ production. This approach assumes that some fraction F_C of the $c\bar{c}$ pairs produced in perturbative QCD with a pair mass below that of the $D\overline{D}$ pair mass threshold will go on mass shell as a J/ψ,

$$\sigma_{\mathrm{CEM}}(pp) = F_C \sum_{i,j} \int_{4m^2}^{4m_H^2} ds \int dx_1 dx_2 F_i^p(x_1, \mu_F^2, k_{T_1})$$
$$\times F_j^p(x_2, \mu_F^2, k_{T_2}) \hat{\sigma}_{ij}(\hat{s}, \mu_F^2, \mu_R^2), \qquad (3)$$

where $ij = gg$, $q\bar{q}$, or $q(\bar{q})g$ and $\hat{\sigma}_{ij}(\hat{s}, \mu_F^2, \mu_R^2)$ is the partonic cross section for the initial state ij evaluated at factorization scale μ_F and renormalization scale μ_R. (Note that the $q(\bar{q})g$ process only enters at next-to-leading order in α_s.) The parton densities are written here to include intrinsic k_T, required to keep the pair cross section finite as $p_T \to 0$. They are assumed to factorize into the normal parton densities in collinear factorization and a k_T-dependent function,

$$F^p(x, \mu_F^2, k_T) = f^p(x, \mu_F^2) G_p(k_T). \qquad (4)$$

The CT10 proton parton densities [38] are employed in the calculations of $f^p(x, \mu_F^2)$.

The charm quark mass, factorization scale and renormalization scale determined from a fit to the total $c\bar{c}$ cross section at NLO in Ref. [39] are employed here, $(m, \mu_F/m_T, \mu_R/m_T) = (1.27 \pm 0.09 \text{ GeV}, 2.1^{+2.55}_{-0.85}, 1.6^{+0.11}_{-0.12})$ where μ_F is the factorization scale and μ_R is the renormalization scale. The scale factors, μ_F and μ_R, are defined relative to the transverse mass of the pair, $\mu_{F,R} \propto m_T = (m^2 + p_T^2)^{1/2}$ where the p_T is the $c\bar{c}$ pair p_T, $p_T^2 = 0.5(p_{T_Q}^2 + p_{T_{\bar{Q}}}^2)$. At LO in the CEM, the J/ψ p_T is zero. Thus, the calculated p_T distribution is LO while the x_F distribution is at NLO.

The improved color evaporation model has recently been developed [36] and extended to studies of quarkonium polarization [40–43] in hadroproduction. The change in the mass integration range and in the definition of the p_T of the quarkonium state changes the $\psi(2S)$ p_T distribution relative to the J/ψ at high p_T and, due to the narrower integration range, increases F_C for J/ψ in the ICEM by $\approx 40\%$ [36]. The J/ψ p_T distributions are compatible with each other in the two approaches, see Ref. [42] for a comparison.

Calculations in the CEM were carried out at next-to-leading order (NLO) in the heavy flavor cross section using the exclusive NLO $Q\bar{Q}$ production code HVQMNR [44] after imposing a cut on the pair invariant mass. This exclusive calculation is applied because it can keep track of both the c and $\bar{c}$ quarks that constitute the J/ψ. However, to keep the p_T distribution finite as $p_T \to 0$, the calculations require augmentation by k_T broadening, as described in more detail below.

Results on open heavy flavors at fixed-target energies indicated that some level of transverse momentum broadening was needed to obtain agreement with the fixed-target data after fragmentation was applied [45]. Broadening has typically been modeled by including intrinsic transverse momentum, k_T, smearing to the parton densities and plays the role of low-p_T QCD resummation [46].

In the HVQMNR code, an intrinsic k_T is added in the final state, rather than the initial state, as was previously done for Drell-Yan production [46]. When applied in the initial-state it multiplies the parton distribution functions for both hadrons, assuming the x and k_T dependencies factorize in the parton distributions, as in Eq. (4). If the k_T kick is not too large, it does not matter whether the k_T dependence is added in the initial or final state.

Because the kick is employed in the final state, effectively the factors $G_p(k_T)$ in Eq. (4) for each parton is replaced by

$$g_p(k_T) = G_p(k_{T_1}) G_p(k_{T_2}). \tag{5}$$

A Gaussian is employed to define $g_p(k_T)$ [45],

$$g_p(k_T) = \frac{1}{\pi \langle k_T^2 \rangle_p} \exp\left(-k_T^2/\langle k_T^2 \rangle_p\right). \tag{6}$$

In Ref. [45], $\langle k_T^2 \rangle_p = 1 \text{ GeV}^2$ was chosen to describe the p_T dependence of fixed-target charm production.

The broadening is applied by first boosting the produced $c\bar{c}$ pair (plus light parton at NLO) to its rest frame from its longitudinal center-of-mass frame. The intrinsic transverse momenta, $\vec{k}_{T1}$ and $\vec{k}_{T2}$, of the incident partons are chosen at random with k_{T1}^2 and k_{T2}^2 distributed according to Eq. (6), preserving the total kick. Boosting back to the original frame changes the initial transverse momentum of the $c\bar{c}$ pair from $\vec{p}_T$ to $\vec{p}_T + \vec{k}_{T1} + \vec{k}_{T2}$. If the k_T was applied to the incident parton distributions, instead of the final-state $c\bar{c}$ pair, there would be no difference at LO. At NLO there can also be a light parton in the final state, making the correspondence inexact. The difference between the two implementations should be small if $\langle k_T^2 \rangle \leqslant 2 \text{ GeV}^2$, as is the case here [45]. While the rapidity distributions are independent of the intrinsic k_T, there will be some modification of the x_F distribution because $x_F = (2m_T/\sqrt{s_{NN}}) \sinh y$ and $m_T = (p_T^2 + m^2)^{1/2}$.

The effect of the k_T kick on the p_T distribution can be expected to decrease as $\sqrt{s}$ increases because the average p_T also increases with energy. However, the value of $\langle k_T^2 \rangle_p$ is assumed to increase with $\sqrt{s}$ so that effect remains particularly important for low-p_T production at higher energies. The energy dependence of $\langle k_T^2 \rangle$ in Ref. [39] is

$$\langle k_T^2 \rangle_p = \left[1 + \frac{1}{n} \ln\left(\frac{\sqrt{s_{NN}}(\text{GeV})}{20 \text{GeV}}\right)\right] \text{GeV}^2 \tag{7}$$

with $n = 12$ for J/ψ production [39]. At the energy of the SeaQuest experiment, $\sqrt{s_{NN}} = 15.4$ GeV, $\langle k_T^2 \rangle_p = 0.97 \text{ GeV}^2$. At $\sqrt{s_{NN}} = 38.8$ GeV, the energy at which the E866 data were taken, $\langle k_T^2 \rangle_p$ rises to 1.05 GeV^2.

Figure 1 shows the x_F and p_T distributions for J/ψ production in $p + p$ collisions in the CEM at 120 GeV. The mass and scale uncertainties are calculated using the one standard deviation uncertainties on the quark mass and scale parameters. If the central, upper and lower limits of $\mu_{R,F}/m_T$ are denoted as C, H, and L respectively, the seven sets used to determine the scale uncertainty are $\{(\mu_F/m_T, \mu_F/m_T)\} = \{(C, C), (H, H), (L, L), (C, L), (L, C), (C, H), (H, C)\}$. The uncertainty band can be obtained for the best fit sets [39] by adding the uncertainties from the mass and scale variations in quadrature. The envelope contained by the resulting curves,

$$\frac{d\sigma_{\max}}{dX} = \frac{d\sigma_{\text{cent}}}{dX} + \sqrt{\left(\frac{d\sigma_{\mu,\max}}{dX} - \frac{d\sigma_{\text{cent}}}{dX}\right)^2 + \left(\frac{d\sigma_{m,\max}}{dX} - \frac{d\sigma_{\text{cent}}}{dX}\right)^2}, \tag{8}$$

$$\frac{d\sigma_{\min}}{dX} = \frac{d\sigma_{\text{cent}}}{dX} - \sqrt{\left(\frac{d\sigma_{\mu,\min}}{dX} - \frac{d\sigma_{\text{cent}}}{dX}\right)^2 + \left(\frac{d\sigma_{m,\min}}{dX} - \frac{d\sigma_{\text{cent}}}{dX}\right)^2}, \tag{9}$$

defines the uncertainty on the cross section. The kinematic observables, denoted by X, are x_F and p_T in this case. The calculation labeled "cent" employs the central values of m, μ_F, and μ_R. The calculations with subscript μ keep the mass
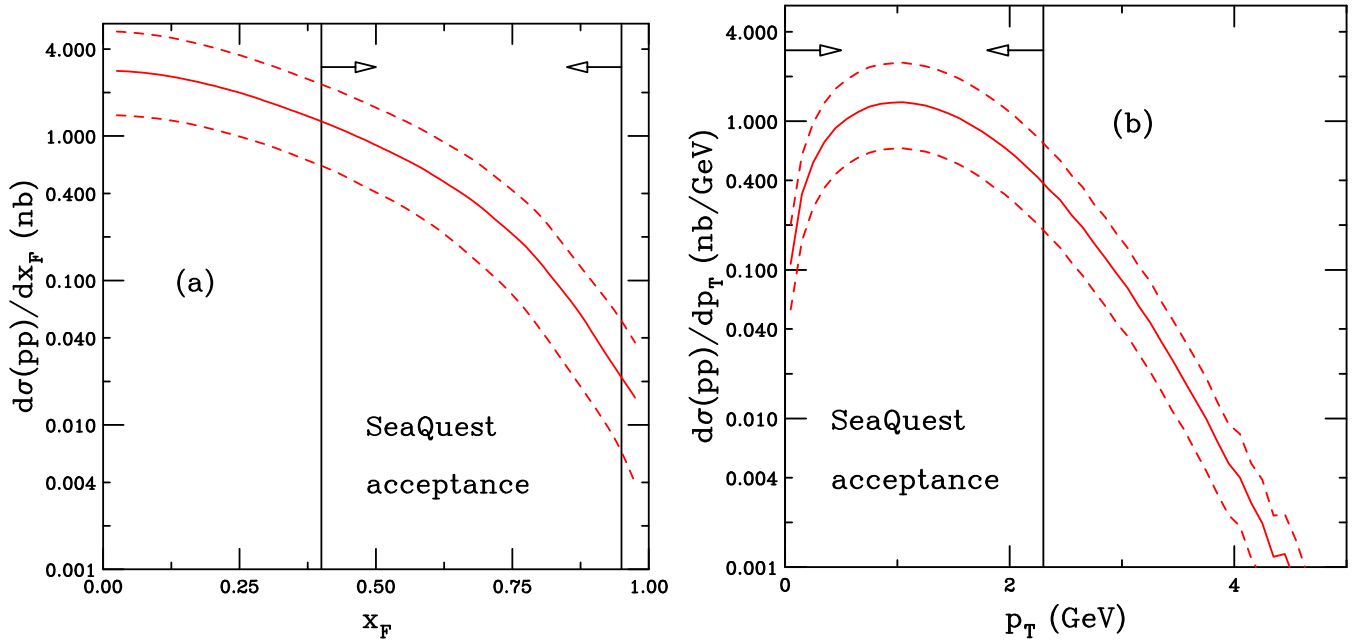
FIG. 1. The J/ψ production cross sections in the CEM in $p + p$ collisions at $\sqrt{s} = 15.4$ GeV as a function of (a) x_F and (b) p_T, integrated over all phase space, are shown. The solid curves show the central values while the dashed curves outline the upper and lower limits of the uncertainty band.

fixed to the central value while the scales are varied. On the other hand, in the calculations with subscript m, the scales are fixed to their central values while the mass is varied between its upper and lower limits. Unless otherwise noted, the calculations employ the central values of the mass and scale factors.

At the center-of-mass energy of the SeaQuest experiment, the J/ψ cross section is still growing rather quickly with $\sqrt{s}$ and the mass uncertainty is dominant. Changing the charm quark mass within its 7% uncertainty can change the forward J/ψ cross section (in the range $0 < x_F < 1$) by almost a factor of two. On the other hand, changing the factorization scale at the relatively large momentum fraction carried by the incident partons, gives a rather small effect on the cross sections, less than 30%.

Note that in the acceptance of the SeaQuest experiment, $0.4 < x_F < 0.95$ and $p_T < 2.3$ GeV, $\approx 22\%$ of the total cross section is captured. In particular, the far-forward acceptance in x_F is in a region where one might expect $q\bar{q}$ or $qg/\bar{q}g$ contributions to heavy flavor production to be non-negligible compared with gg production of J/ψ. Figure 2 shows the ratio of the partial cross sections for each partonic initial state, the squared amplitude weighted by the parton densities, relative to the total cross section. Indeed at $\sqrt{s_{NN}} = 15.4$ GeV, if J/ψ production is broken down into its gg, $q\bar{q}$, and $qg/\bar{q}g$ contributions, the gg contribution is $\approx 80\%$ over the x_F range, integrated over all p_T, while the $q\bar{q}$ and qg contributions are $\approx 25\%$ and $\approx -10\%$ respectively, see Fig. 2(a). The contributions from the production channels change more as a function of p_T, integrated over forward x_F, as shown in Fig. 2(b), As p_T increases the gg and qg contributions become comparable at $p_T \approx 5$ GeV while the $q\bar{q}$ contribution decreases. See Refs. [44,47] for discussions of the relative contributions of the production channels. Also, note that even though the qg

contribution is negative over much of the kinematic range, the total cross section is positive. These results show that in the specific kinematics and the low center-of-mass energy of the SeaQuest experiment, the gg contribution, while it is larger than the other contributions, is not fully dominant. At higher energies, including already at $\sqrt{s_{NN}} = 38.8$ GeV, the energy of the E866 experiment, the gg contribution is larger than 95% of the total due to both the larger gg partonic cross section at high energies and the larger gg luminosity at higher energies and smaller x.

These distributions are not significantly modified in $p + d$ relative to $p + p$ collisions. The $p + d$ cross section is about 1%–2% larger per nucleon than the $p + p$ cross section. This difference can be attributed to the modified valence quark contributions in proton relative to deuterium targets and is non-negligible at the SeaQuest energy because the $q\bar{q}$ contribution is around 25% of the cross section in the SeaQuest acceptance.

B. Nuclear effects on the parton densities

The parton distribution functions in nuclei are modified from those of a free proton. A characteristic dependence of this modification has been determined from deep-inelastic scattering experiments of leptons (electrons, muons, or neutrinos) on nuclei. These leptonic measurements probe only charged partons, leaving the gluon modifications to be inferred through the evolution of the parton densities with scale and momentum sum rules. The characteristic dependence is usually presented as the ratio of the structure function in a heavier nucleus, F_{2A} relative to the structure function in the deuteron, F_{2d}. The deuteron is chosen because it has an equal number of up and down valence quarks between the
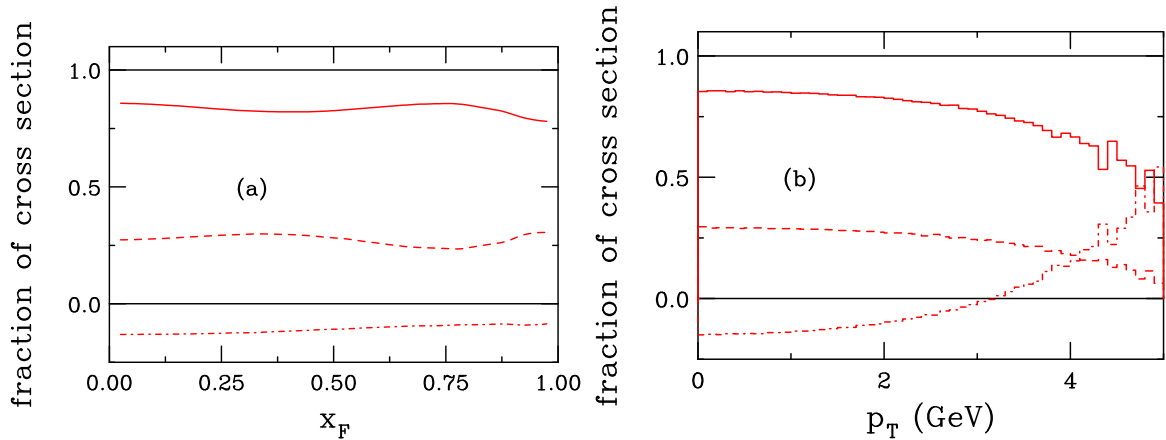
FIG. 2. The contributions to the J/ψ production cross sections in the CEM in $p + p$ collisions at $\sqrt{s} = 15.4$ GeV as a function of (a) x_F and (b) p_T are shown for the gg (solid), $q\bar{q}$ (dashed) and qg (dot-dashed) initial states.

constituent neutron and proton. At high momentum fractions, $x > 0.3$, carried by the interacting parton, there is a depletion in the nucleus relative to a nucleon, known as the European Muon Collaboration (EMC) Effect. At smaller values of x, $x < 0.03$, there is also a depletion, known as shadowing. In the intermediate range of x, bridging the two regions where the ratio $R = F_{2A}/F_{2d} < 1$, there is an enhancement referred to as antishadowing.

A number of global analyses have been made over time by several groups to describe the modification as a function of x and factorization scale μ_F, assuming collinear factorization and starting from a minimum scale, μ_F^0. These analyses have evolved with time, similar to global analyses of the proton parton distribution functions, as more data become available.

Nuclear PDF effects are generally implemented by a parametrization of the modification as a function of x, μ_F, and A so that the k_T-independent proton parton distribution function in Eq. (3) is replaced by the nuclear parton distribution function

$$f_j^A\left(x_2, \mu_F^2\right) = R_j\left(x_2, \mu_F^2, A\right) f_j^p\left(x_2, \mu_F^2\right). \qquad (10)$$

Note that the separate modifications for valence and sea quarks in the case of up and down quarks requires the modification to be applied separately to the valence and sea quark proton distributions. The isospin also needs to be taken into account for the light quark distributions as well to distinguish between proton and neutron contributions.

Here the EPPS16 [48] nPDF parametrization at next-to-leading order in the strong-coupling constant α_s is employed in the calculations. It is available for $A = 12$ (carbon), 56 (iron), and 184 (tungsten) but assumes no modification for the deuteron target.

The EPPS16 analysis used the LHC data from the 2012 $p + $ Pb run at $\sqrt{s_{NN}} = 5.02$ TeV. Data on dijet production, as well as for $W^\pm$ and Z gauge boson data, are still rather sparse but probe much higher scales than previously available from fixed-target nuclear deep-inelastic-scattering experiments. This analysis also included the CHORUS data [49] with neutrino and antineutrino beams. All these additional

data sets gave access to a wide range of scales, $4 \leqslant \mu_F^2 \leqslant 2 \times 10^4$ GeV^2, at relatively large x. They were also sensitive to differences in the valence and sea quark distributions, allowing separation between u_V and d_V and $\bar{u}$ and $\bar{d}$, respectively.

EPPS16 has 20 fit parameters, giving 41 total sets with one central set and 40 error sets. The error sets are determined by varying each parameter individually within one standard deviation of its best-fit value. The uncertainties on the individual quark ratios are calculated by summing the excursions of each of the error sets from the central value in quadrature. The sets cover the range $1.3 < Q < 10\,000$ GeV and $10^{-7} < x < 1$.

The uncertainties on the J/ψ distributions due to EPPS16 are obtained by calculating the J/ψ cross sections with the central set and the 40 error sets and summing the differences in quadrature. The resulting J/ψ uncertainty band deviates from the central cross section on the order of 20%, significantly less than the mass and scale uncertainties shown in Fig. 1.

The EPPS16 ratios for gluons, valence up quarks, and $\bar{u}$ quarks are shown at the J/ψ mass scale in Fig. 3. The central sets, along with the uncertainty bands, are shown for all three targets for gluons [Fig. 3(a)], anti-up quarks [Fig. 3(b)] and valence up quarks [Fig. 3(c)]. The range $x > 0.007$ is emphasized since SeaQuest does not probe the small-x region. Indeed, the average x range probed by SeaQuest is rather narrow and in the range where antishadowing is dominant. To set the limits in x shown in Fig. 3, the momentum fraction x_2 in the nucleus is calculated for $x_F = 0.95$, $p_T = 0$ and $x_F = 0.4$, $p_T = 2.3$ GeV in $2 \to 2$ kinematics where $x_2 = 0.5[-x_F + (x_F^2 + 4m_T^2/s)^{1/2}]$ and $m_T = (m_{J/\psi}^2 + p_T^2)^{1/2}$, assuming that any light final-state parton associated with J/ψ production in the $2 \to 3$ next-to-leading order kinematics has a small effect on the resulting x_2. These combinations of x_F and p_T give the minimum and maximum values of x_2, 0.068 and 0.136, respectively. In the E866 kinematics, the x_2 range probed at high x_F is lower, $x_2 \approx 0.12$ for $x_F = -0.065$, the midpoint of the lowest x_F bin and $x_2 \approx 0.007$ in the highest x_F bin with midpoint $x_F = 0.913$ [6]. Here the lowest value of x_2 probed is an order of magnitude smaller than for high x_F
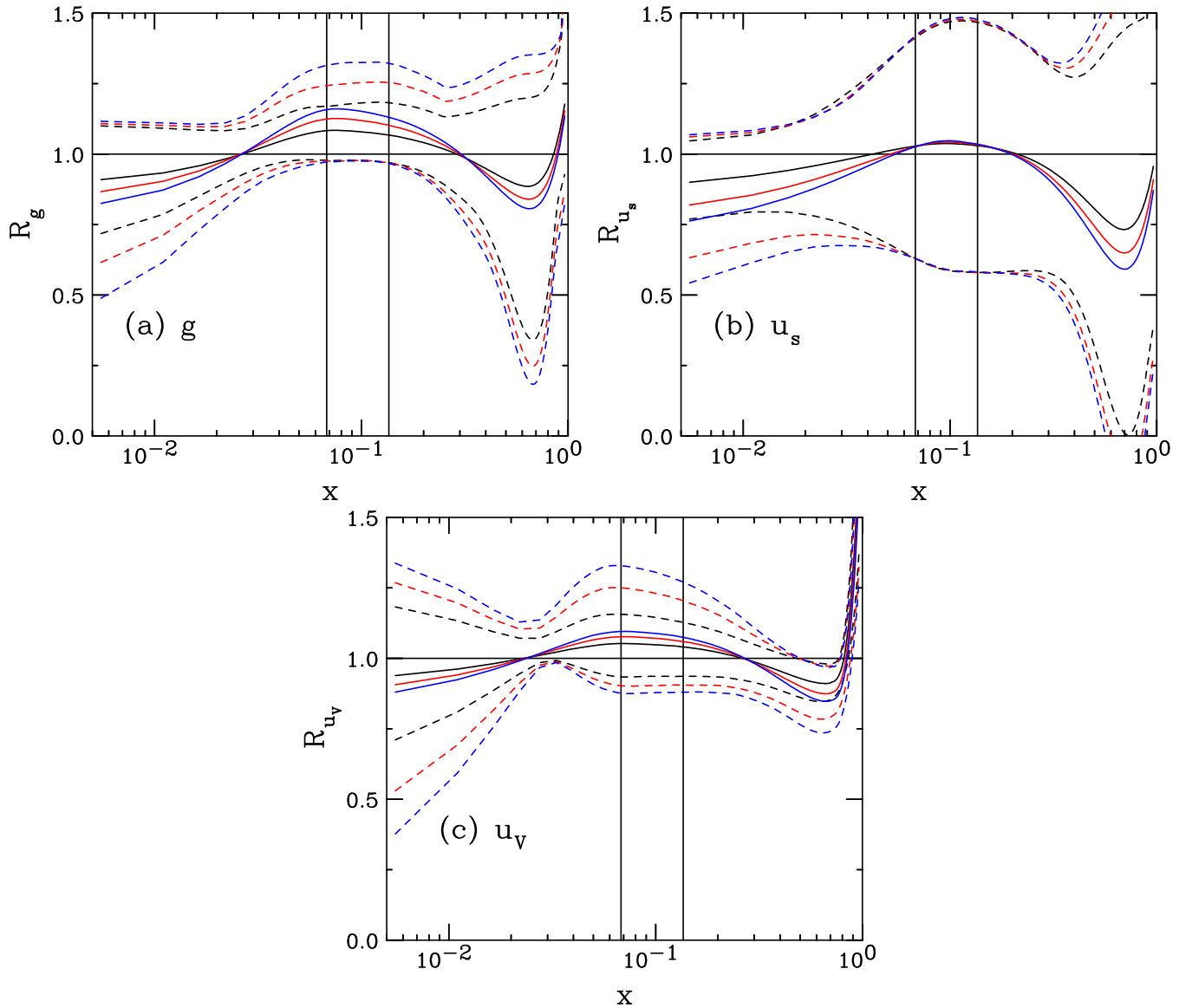
FIG. 3. The EPPS16 ratios, with uncertainties, are shown at the scale of (a) the J/ψ mass for gluons, (b) the up sea quark distribution, and (c) the valence up quark distribution as a function of momentum fraction x. The central set is denoted by the solid curves while the dashed curves give the upper and lower limits of the uncertainty bands. The results are given for $A = 12$ (black), 56 (red), and 184 (blue). The vertical lines indicate the x range of the SeaQuest measurement, $0.068 < x < 0.136$.

at SeaQuest. Thus one can expect antishadowing near $x_F \approx 0$ and shadowing at high x_F in the E866 range.

The ratios are all shown for the J/ψ mass, $\mu_F = m_{J/\psi}$. At this value of the factorization scale, within a factor of three of the minimum scale employed in the EPPS16 fits, $\mu_F = 1.3$ GeV, the uncertainty band is quite large.

The fixed-target neutrino deep-inelastic-scattering data and the gauge boson data from the LHC reveal differences between the valence and sea quark ratios. The nuclear modification is weaker for d_V than for u_V while there is no antishadowing for $\bar{d}$. On the other hand, the $\bar{u}$ ratio shows antishadowing on a level similar to the valence quarks, albeit over a narrower range in x. Only the $\bar{u}$ and u_V modifications are shown in Fig. 3. Examples of the sea quark and valence quark ratios are shown because SeaQuest is in a kinematic

region where J/ψ production is not dominated by production via the gg channel, see Fig. 2.

Finally, it is worth noting that these modifications assume minimum bias collisions, averaging over the volume of the nucleus. Measurements of J/ψ production in $p + $Pb collisions at much lower x such as of the ALICE Collaboration have been shown as a function of collision centrality, as determined by event multiplicity [50]. These results exhibit a clear dependence on where the probe impacts the nucleus, for example, in peripheral collisions, closer to the "edge" of the nucleus where there might be only one nucleon in the path of the proton or more central collisions where the proton may encounter multiple nucleons [51,52]. It would be interesting to see whether similar modifications could be observed in high-statistics fixed-target measurements such as at SeaQuest.

C. Nuclear absorption in *pA* interactions

In $p + A$ collisions, the proto-J/ψ produced in the initial parton interactions may further interact with nucleons and be dissociated or absorbed before it can escape the target, referred to as nuclear absorption. The effect of nuclear absorption alone on the J/ψ production cross section in $p + A$ collisions may be expressed as [25]

$$\sigma_{pA} = \sigma_{pN} S_A^{\text{abs}} = \sigma_{pN} \int d^2 b \int_{-\infty}^{\infty} dz \rho_A(b, z) S^{\text{abs}}(b) \quad (11)$$

$$= \sigma_{pN} \int d^2 b \int_{-\infty}^{\infty} dz \rho_A(b, z)$$

$$\times \exp \left\{ - \int_z^{\infty} dz' \rho_A(b, z') \sigma_{\text{abs}}(z' - z) \right\}, \quad (12)$$

where b is the impact parameter, z is the $c\bar{c}$ production point, $S^{\text{abs}}(b)$ is the nuclear absorption survival probability, and $\sigma_{\text{abs}}(z' - z)$ is the nucleon absorption cross section. Even though the absorption cross section used in this work is assumed to be constant, it is written as a function of the path length through the nucleus in Eq. (12) because other functional forms have previously been assumed, see, e.g., Ref. [53]. Expanding the exponent in Eq. (12), integrating, and re-exponentiating the results assuming A is large leads to Eq. (1) with $S_A^{\text{abs}} = A^{\alpha}$ and $\alpha = 1 - 9\sigma_{\text{abs}}/(16\pi r_0^2)$ [25].

There have been many studies of the absorption mechanism of the J/ψ in nuclei and the cross section obtained in various model studies depends on whether the J/ψ is assumed to be produced inside or outside the target and whether it is produced as a color singlet or color octet. For comparison of results assuming different absorption scenarios, see, for example, Refs. [32,53–55] and references therein.

The extracted absorption cross section also depends on which cold nuclear matter effects were taken into account. If one assumes only absorption, the cross section could be underestimated at low energies because antishadowing effects have been neglected. At energies where antishadowing dominates, a larger effective absorption cross section is needed to reach the level of measured suppression in $p + A$ relative to $p + p$ collisions, as discussed in Ref. [54]. In that reference, the effective absorption cross section was extracted for each measured x_F or rapidity point for several nPDF parametrizations available at the time. While the effective absorption showed some dependence on the chosen nPDF parametrization, the authors were able to discern some trends. At midrapidity or $x_F \approx 0$, absorption was generally largest and was seen to decrease forward of this central region, at least up to a point. Experiments such as Fermilab's E866 experiment [6] at $\sqrt{s_{NN}} = 38.8$ GeV or the NA3 collaboration [1] at CERN with $\sqrt{s_{NN}} = 19.4$ GeV showed a strong increase in effective absorption for more forward x_F, $x_F > 0.3$ [54]. It was also noted, including by the E866 Collaboration [6], that although high x_F also corresponds to low x_2 and the shadowing region, results at different energies did not scale with x_2, demonstrating that shadowing could not be the dominant effect in that region. Other effects such as energy loss in cold matter were speculated to lead to the observed behavior.

Based on the midrapidity results, an energy-dependent effective absorption cross section was obtained employing the available data [54]. Extrapolating the findings back to 120 GeV gives $7 \leqslant \sigma_{\text{abs}} \leqslant 9$ mb. A value of 9 mb is used here and is compared with results with no nucleon absorption, $\sigma_{\text{abs}} = 0$ and $\alpha = 1$. When comparing with the E866 data, a lower value, $\sigma_{\text{abs}} = 5$ mb, is used, consistent with the findings in Ref. [54].

Even though J/ψ absorption may be inextricably entangled with other cold nuclear matter effects in hadroproduction, it may be possible to make an independent measurement of the J/ψ-nucleon total cross section, effectively the absorption cross section, from measurement of the A dependence in photoproduction. Such an experiment was performed at the Stanford Linear Accelerator Center (SLAC) at 20 GeV [56], giving a value of $3.5 \pm 0.8 \pm 0.5$ mb, lower than estimates from hadroproduction at higher energies [54]. A new experiment of the A dependence at similar energies would be useful [57], especially if the coherent and incoherent contributions could be separated. Measurements of J/ψ production in ultraperipheral collisions, while not shedding new light on absorption by nucleons, can provide additional constraints on the nuclear gluon parton densities. Measurements reported by ALICE [58,59] and CMS [60] have already put some constraints on the gluon density in the nucleus at low x.

Absorption by comoving particles, whether characterized as hadrons or partons, has been included in some calculations of cold nuclear matter effects [61]. This type of suppression has not been included separately here because it has been shown to have the same nuclear dependence in minimum-bias collisions [62].

D. k_T broadening

The effect and magnitude of intrinsic k_T broadening on the J/ψ p_T distribution in $p + p$ collisions was discussed in Sec. II A. Here further broadening due to the presence of a nuclear target is considered. One might expect that a higher intrinsic k_T is required in a nuclear medium relative to that in $p + p$ due to multiple scattering in the nucleus, known as the Cronin effect [63]. The effect is implemented by replacing $g_p(k_T)$ in Eq. (5) by $g_A(k_T)$ where $\langle k_T \rangle_p$ is replaced by $\langle k_T \rangle_A$ in Eq. (6).

The total broadening in a nucleus relative to a nucleon can be expressed as

$$\langle k_T^2 \rangle_A = \langle k_T^2 \rangle_p + \delta k_T^2. \quad (13)$$

The same expression for δk_T^2 used in Ref. [64], based on Ref. [65], is employed here,

$$\delta k_T^2 = (\langle \nu \rangle - 1) \Delta^2(\mu). \quad (14)$$

The strength of the broadening, $\Delta^2(\mu)$, depends on the interaction scale [65],

$$\Delta^2(\mu) = 0.225 \frac{\ln^2(\mu/\text{GeV})}{1 + \ln(\mu/\text{GeV})} \text{GeV}^2. \quad (15)$$

The scale at which the broadening is evaluated is taken to be $\mu = 2m_c$ [64]. The scale dependence suggests that one might

expect a larger k_T kick in the nucleus for bottom quarks than charm quarks.

The size of the effect depends on the number of scatterings the incident proton could undergo while passing through a nucleus. This is given by $\langle \nu \rangle - 1$, the number of collisions, less the first collision. The number of scatterings strongly depends on the impact parameter of the proton with respect to the nucleus. However, in minimum-bias collisions, the impact parameter is averaged over all possible paths. The average number of scatterings is

$$\langle \nu \rangle = \sigma_{pp}^{\rm in} \frac{\int d^2 b T_A^2(b)}{\int d^2 b T_A(b)} = \frac{3}{2} \rho_0 R_A \sigma_{pp}^{\rm in}, \tag{16}$$

where $T_A(b)$ is the nuclear profile function, $T_A(b) = \int_{-\infty}^{\infty} dz \rho_A(b, z)$, and ρ_A is the nuclear density distribution. An average nuclear density, $\rho_0 = 0.16/\text{fm}^3$, is assumed for a spherical nucleus of radius $R_A = 1.2A^{1/3}$; and $\sigma_{pp}^{\rm in}$ is the inelastic $p + p$ cross section, ≈ 32 mb at fixed-target energies.

With the given values of ρ_0 and $\sigma_{pp}^{\rm in}$ in Eq. (16) and $\Delta^2(\mu = 2m_c) = 0.101$ GeV^2 from Eq. (15),

$$\delta k_T^2 \approx (0.92A^{1/3} - 1) \times 0.101 \text{ GeV}^2. \tag{17}$$

For carbon, iron, and tungsten targets, $\delta k_T^2 = 0.1, 0.25,$ and 0.39 GeV^2, respectively. This gives an average broadening in the nucleus of $\langle k_T^2 \rangle_A = 1.07, 1.22,$ and 1.36 GeV^2 for the SeaQuest targets. The change in $\langle k_T^2 \rangle$ between carbon and

tungsten targets is similar to that observed for J/ψ production in other fixed-target experiments [8]. That work also observed that this relative broadening was independent of center-of-mass energy.

At the higher energy of the E866 experiment, $\langle k_T^2 \rangle_p$ increases to 1.05 GeV^2. The beryllium, iron and tungsten targets are effectively identical to the SeaQuest targets but the higher energy increases the average broadening to $\langle k_T^2 \rangle_A = 1.15, 1.3,$ and 1.44 GeV^2, respectively.

The effect of k_T broadening in nuclei, relative to the proton, is to reduce the ratio $p + A/p + p$ or $p + A/p + {\rm d}$ at low p_T and enhance it at high p_T. Because x_F depends on m_T, one can expect a small effect as a function of x_F while a more significant one should be seen as a function of p_T.

III. INTRINSIC CHARM

The wave function of a proton in QCD can be represented as a superposition of Fock state fluctuations, e.g., $|uudg\rangle$, $|uudq\bar{q}\rangle$, $|uudQ\bar{Q}\rangle$, ...of the $|uud\rangle$ state. When the projectile scatters in the target, the coherence of the Fock components is broken and the fluctuations can hadronize [16,17,66]. These intrinsic $Q\bar{Q}$ Fock states are dominated by configurations with equal rapidity constituents. Thus the intrinsic heavy quarks carry a large fraction of the projectile momentum [16,17].

The frame-independent probability distribution of a five-particle $c\bar{c}$ Fock state in the proton is

$$dP_{\rm ic5} = P_{\rm ic5}^0 N_5 \int dx_1 \cdots dx_5 \int dk_{x1} \cdots dk_{x5} \int dk_{y1} \cdots dk_{y5} \frac{\delta\left(1 - \sum_{i=1}^{5} x_i\right)\delta\left(\sum_{i=1}^{5} k_{xi}\right)\delta\left(\sum_{i=1}^{5} k_{yi}\right)}{\left(m_p^2 - \sum_{i=1}^{5}\left(\widehat{m}_i^2/x_i\right)\right)^2}, \tag{18}$$

where $i = 1, 2, 3$ are the interchangeable light quarks (u, u, d) and $i = 4$ and 5 are the c and $\bar{c}$ quarks respectively. Here N_5 normalizes the $|uudc\bar{c}\rangle$ probability to unity and $P_{\rm ic5}^0$ scales the unit-normalized probability to the assumed intrinsic charm content of the proton. The δ functions conserve longitudinal (z) and transverse (x and y) momentum. The denominator of Eq. (18) is minimized when the heaviest constituents carry the largest fraction of the longitudinal momentum, $\langle x_Q \rangle > \langle x_q \rangle$.

Note that only this five-particle Fock state of the proton is considered here since it gives the most forward x_F production of J/ψ from intrinsic charm. One can also consider higher Fock components such as $|uudc\bar{c}q\bar{q}\rangle$ but these will reduce the average momentum fraction of the J/ψ and also enter at lower probabilities, see, e.g., Refs. [67] for examples of charm hadron distributions from higher Fock states.

Heretofore, only the x_F dependence of the J/ψ from the five-particle Fock state has been considered. In this case average values for the transverse masses of the constituent quarks, $\widehat{m}_i^2 = m_i^2 + k_{Ti}^2$, can be used. Previously, $\widehat{m}_q = 0.45$ GeV and $\widehat{m}_c = 1.8$ GeV were chosen [31]. In this case, the J/ψ x_F distribution can be calculated by assuming simple coalescence of the c and $\bar{c}$ in a single state, represented in Eq. (18) by the addition of a δ function, $\delta(x_F - x_c - x_{\bar{c}})$, for the longitudinal z direction. We can relate the summed x_c and $x_{\bar{c}}$ momentum fractions to the x_F of the J/ψ by

assuming that it is brought on-shell by a soft scattering with the target.

In this work, the p_T distribution of the J/ψ from such a Fock state is calculated explicitly for the first time. Thus the k_x and k_y integrals are also represented in Eq. (18). To simplify the calculations, it is assumed that the transverse momentum of the J/ψ, p_T, is in the x direction only. This introduces two δ functions to Eq. (18), $\delta(p_T - k_{xc} - k_{x\bar{c}})$ and $\delta(k_{yc} + k_{y\bar{c}})$.

Employing these δ functions, the longitudinal momentum fraction of the $\bar{c}$ can be integrated, as well as the transverse momentum of the $\bar{c}$ quark in the proton, leaving the light quark x and $\vec{k}$ as well as that of the c quark to be integrated numerically.

The J/ψ x_F and p_T probability distributions from intrinsic charm are shown in Fig. 4. The distributions are normalized to unity. How this normalized probability distribution is converted into a cross section for J/ψ production by intrinsic charm is explained shortly. Results are shown for different values of k_T for the light and charm quarks in the proton.

As shown in Fig. 4(a), the x_F dependence is effectively independent of the chosen k_T limits. The average x_F of the distribution is 0.53, almost exactly the same as previous calculations assuming constant values of $\widehat{m}_q = 0.45$ GeV and $\widehat{m}_c^2 = 1.8$ GeV [31]. The charm quark x_c distribution obtained by integrating over the momenta of the other four partons
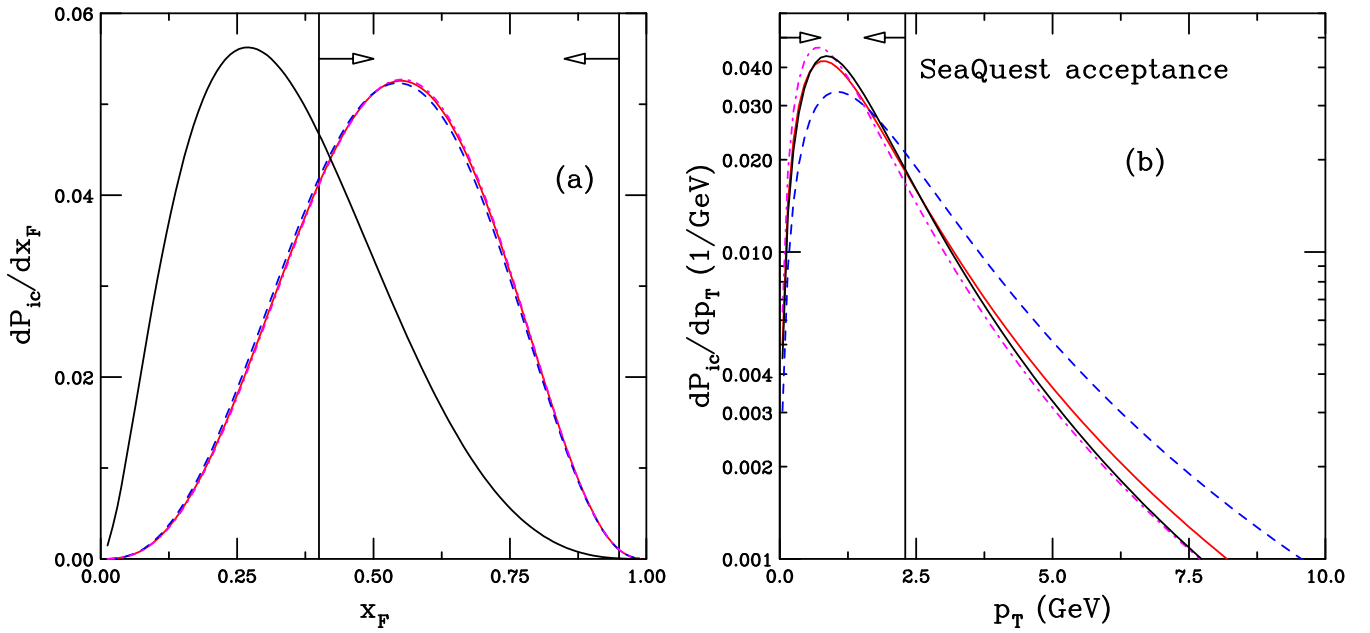
FIG. 4. The probability distributions for J/ψ production from a five-particle proton Fock state as a function of (a) x_F and (b) p_T. The results are shown for different values of the k_T range for the light and charm quarks. The red curve employs the default values, $k_q^{max} = 0.2$ GeV and $k_c^{max} = 1.0$ GeV while the blue dashed curve increases k_q^{max} and k_c^{max} by a factor of two and the dot-dashed magenta curve employs half the values of k_q^{max} and k_c^{max}. The solid black curve shows the x and p_T distributions for a single charm quark from the state.

in the Fock state, assuming the quark is liberated from the projectile proton by a soft interaction. It has an average value of $x_c = 0.34$, slightly larger than half that of the J/ψ.

The p_T distributions, on the other hand, show a significant dependence on the range of k_T integration. The chosen default values are $k_q^{max} = 0.2$ GeV and $k_c^{max} = 1.0$ GeV, shown by the red curve in Fig. 4(b). Note that these limits apply to both the x and y directions of the transverse momentum. The charm quark distribution, with these same default values for the range of integration, is given by the black curve.

If the limits of the integration range are doubled to $k_q^{max} = 0.4$ GeV and $k_c^{max} = 2.0$ GeV, the p_T distribution is broadened, see the blue dashed curve in Fig. 4(b), while halving the integration range to 0.1 GeV and 0.5 GeV for the light and charm quarks, respectively, results in the dot-dashed magenta curve. The average J/ψ p_T resulting from these values of k_i^{max} are 2.06, 2.48, and 1.90 GeV for the default range, doubling the range, and halving the range, respectively. The average p_T of the charm quark in the default integration range is 2.00 GeV.

The shape of the p_T distribution from intrinsic charm also depends on the chosen quark masses. Increasing the quark masses broadens the p_T distribution further. For example, choosing $m_c = 1.5$ GeV makes the J/ψ p_T distribution broader than that of the charm quark distribution shown in Fig. 4(b). On the other hand, reducing the light quark mass to 20 MeV, closer to the current quark mass, results in a more steeply falling J/ψ p_T distribution than that obtained by taking $k_q^{max} = 0.1$ GeV and $k_c^{max} = 0.5$ GeV.

It is notable that the J/ψ p_T distribution from intrinsic charm is considerably broader than that of the J/ψ calculated

with the CEM, shown in Fig. 1(b). This can be easily understood, even when an average $\langle k_T \rangle^2 \approx 1$ GeV^2 is employed with the CEM, when one considers the two sources.

In perturbative QCD, the p_T range depends on the center-of-mass energy with a limit of $p_T \sim \sqrt{s_{NN}}/2$ at $x_F = 0$ for massless partons and less for massive quarks, where p_T is replaced by m_T. Leading order $2 \rightarrow 2$ scattering is also assumed for this estimate, leading to $p_T \leqslant 7.2$ GeV in the massless case and $p_T \leqslant 6.5$ GeV for the J/ψ in the CEM. In addition, since the initial partons taking part in the interaction come from two different hadrons, one from the projectile and the other from the target, at least one of them will carry a much smaller fraction of the momentum that the intrinsic charm quarks in the proton Fock state.

On the other hand, when the J/ψ arises from an intrinsic charm state of the proton, according to Eq. (18), there is no energy limit on the p_T distribution other than that imposed by momentum conservation. The J/ψ kinematics all come from the incident proton. Only a soft interaction with the target is sufficient to disrupt the Fock state and bring the J/ψ on mass shell.

Even though intrinsic charm may dominate at higher p_T for the SeaQuest energy and kinematics, at higher energies, the J/ψ cross section from perturbative QCD will be significantly higher and the average p_T of the CEM calculation grows with energy, along with the intrinsic k_T kick imparted to the J/ψ at low p_T, see Eq. (7), while the J/ψ p_T distribution from intrinsic charm distribution will not change. In particular, at colliders, the acceptance is generally around midrapidity (low x_F) and the largest part of the intrinsic charm contribution is thus outside the detector acceptance and detection of intrinsic charm is less favorable.

The intrinsic charm production cross section from the $|uudc\bar{c}\rangle$ component of the proton can be written as

$$\sigma_{ic}(pp) = P_{ic5}\sigma_{pN}^{in}\frac{\mu^2}{4\widehat{m}_c^2}. \qquad (19)$$

The factor of $\mu^2/4\widehat{m}_c^2$ arises from the soft interaction which breaks the coherence of the Fock state where $\mu^2 = 0.1$ GeV^2 is assumed, see Ref. [31], and $\sigma_{pN}^{in} = 30$ mb is appropriate for the SeaQuest energy. Employing this cross section for charm production from the Fock state, the J/ψ contribution is assumed here to be calculated by scaling Eq. (19) by the same factor, F_C, used to scale the CEM calculation to obtain the inclusive J/ψ cross section from the $c\bar{c}$ cross section in Eq. (3),

$$\sigma_{ic}^{J/\psi}(pp) = F_C\sigma_{ic}(pp). \qquad (20)$$

The nuclear dependence of the intrinsic charm contribution is assumed to be the same as that extracted for the nuclear surface-like component of J/ψ dependence by the NA3 Collaboration [1] in Eq. (2), so that

$$\sigma_{ic}^{J/\psi}(pA) = \sigma_{ic}^{J/\psi}(pp)A^\beta \qquad (21)$$

with $\beta = 0.71$ [1] for a proton beam.

To represent the uncertainties on intrinsic charm, several values of the intrinsic charm probability, P_{ic5}^0, are employed. The EMC charm structure function data is consistent with $P_{ic5}^0 = 0.31\%$ for low energy virtual photons but P_{ic5}^0 could be as large as 1% for the highest virtual photon energies [19,68]. For a lower limit, a probability of 0.1% is used. All three results are generally shown in Sec. IV unless otherwise noted.

In this work, the formulation for intrinsic charm in the proton wave function postulated by Brodsky and collaborators in Refs. [16,17] has been adapted. Other variants of the intrinsic charm distribution in the proton exist, including meson-cloud models where the proton fluctuates into a $\overline{D}(u\bar{c})\Lambda_c(udc)$ state [69–72] and a sea-like distribution [73,74]. Intrinsic charm has also been included in global analyses of the parton densities [73–77]. The range of P_{ic5}^0 explored here is consistent with the results of the global analyses. For more details of these other works, see the review of Ref. [78]. (See Ref. [79] for a discussion of a possible kinematic constraint on intrinsic charm in deep-inelastic scattering.) New evidence for a finite charm quark asymmetry in the nucleon wave function from lattice gauge theory, consistent with intrinsic charm, was presented in Ref. [80]. See also the recent review in Ref. [81] for more applications of intrinsic heavy quark states.

IV. RESULTS

The first part of this section presents the results for the nuclear suppression factor,

$$R_{pA} = \frac{2}{A}\frac{\sigma_{pA}}{\sigma_{pd}}, \qquad (22)$$

where the cross section per nucleon in a nuclear target is compared with that of the deuteron target, in the SeaQuest kinematics. The relative per nucleon cross sections are a more straightforward way to present the nuclear dependence

than using the exponent α as was done previously. Using the deuteron target reduces the potential, albeit small, isospin dependence of the ratios.

The calculations shown here are all in the x_F and p_T bins defined by SeaQuest [33]. The calculated points shown in the figures are placed at the arithmetic center of the bin rather than a cross-section-weighted center. Changing the location of the calculated points within the bins could slightly modify the shape of the x_F and p_T dependence in this section but not enough to alter any conclusions. Because the SeaQuest data have not yet been submitted for publication, the calculations shown here cannot yet be compared with data.

Section IV A shows the results with cold nuclear matter effects on the perturbative QCD contribution alone while Sec. IV B includes intrinsic charm, both without and with nuclear absorption on the pQCD contribution. Results are calculated both as a function of x_F and p_T and are shown for all three nuclear targets: $A = 12$ (carbon); $A = 56$ (iron); and $A = 184$ (tungsten).

Section IV C shows calculations compared with the E866 results for α reported in Ref. [6]. Because their reported α combines results from all three targets (beryllium, iron, and tungsten), the value of α is calculated from Eq. (1) for each target, $\alpha = \ln(\sigma_{pA}/\sigma_{pp})/\ln(A)$, and averaged over all three targets.

A. R_{pA} from perturbative quantum chromodynamics effects alone

The focus of the discussion in this section is on only the nuclear effects described in Sec. II. In this case, the cross sections employed in the calculation of R_{pA} are

$$\sigma_{pA} = \sigma_{CEM}(pA)$$
$$= S_A^{abs}F_C\sum_{i,j}\int_{4m^2}^{4m_H^2}ds\int dx_1dx_2 F_i^p(x_1,\mu_F^2,k_T)F_j^A$$
$$\times (x_2,\mu_F^2,k_T)\hat{\sigma}_{ij}(\hat{s},\mu_F^2,\mu_R^2), \qquad (23)$$

where

$$F_j^A(x_2,\mu_F^2,k_T) = R_j(x_2,\mu_F^2,A)f_j(x_2,\mu_F^2)G_A(k_T), \qquad (24)$$

$$F_i^p(x_1,\mu_F^2,k_T) = f_i(x_1,\mu_F^2)G_p(k_T). \qquad (25)$$

In the case of the deuteron target, $R_j \equiv 1$ in EPPS16, and $\delta k_T^2 = 0$ in Eq. (14) so that $g_A(k_T) = g_p(k_T)$. It is also assumed that $\sigma_{abs} = 0$ since the proton and neutron in the deuteron are far separated so the incident proton is likely to interact with only one of the two nucleons in the deuteron. Thus $\sigma_{pd} = 2\sigma_{CEM}(pp)$. As was the case in Eq. (5), here the broadening is applied as

$$g_A(k_T) = G_p(k_{T_1})G_A(k_{T_2}), \qquad (26)$$

discussed in Sec. II D. Results are shown in Fig. 5 as a function of x_F and in Fig. 6 as a function of p_T for effects on the three nuclear targets.

The effects are added sequentially in these figures. Only nPDF effects are common to all the calculated ratios. These nPDF results are presented with the central best-fit set given by the solid curves while the uncertainties added in quadrature
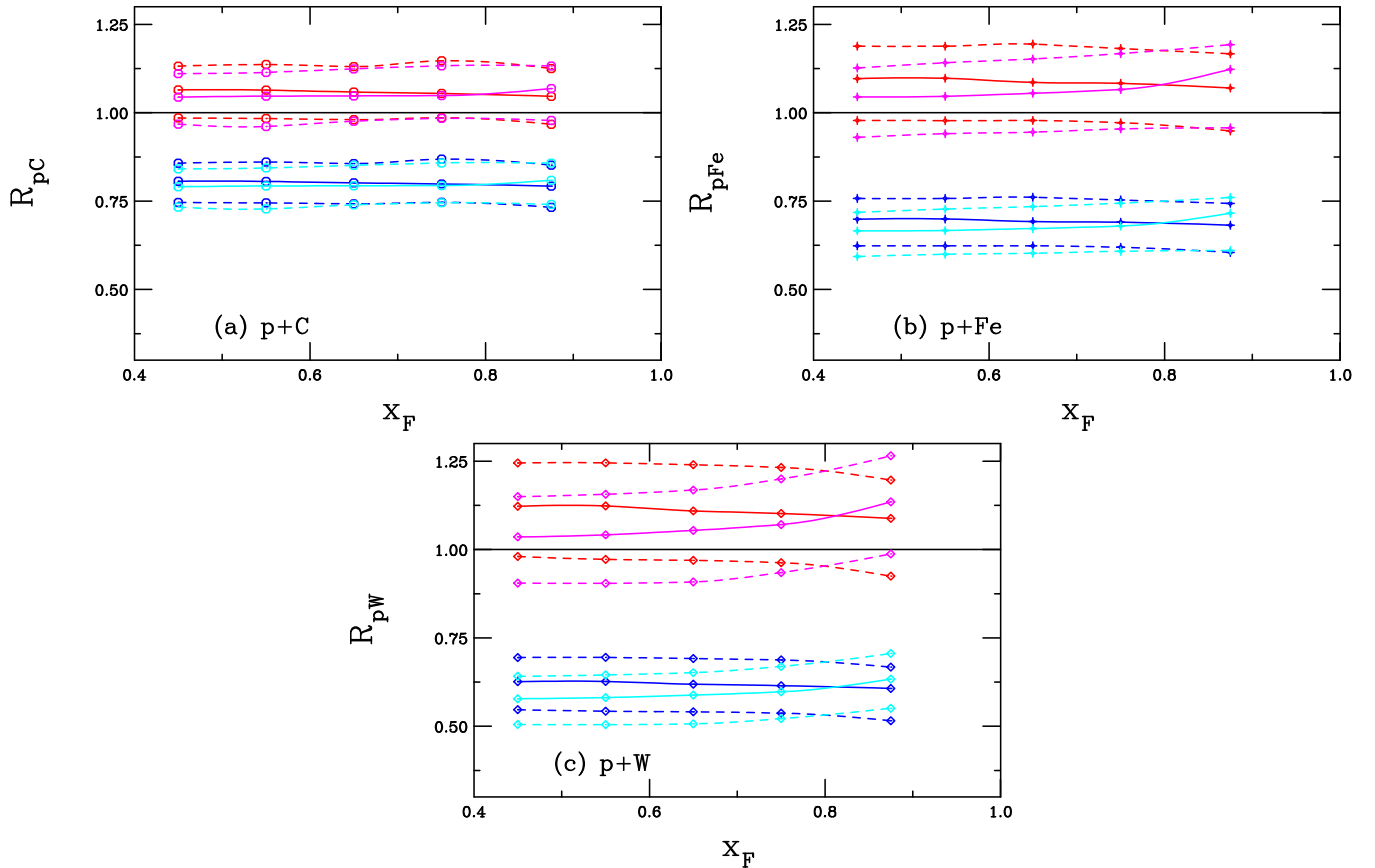
FIG. 5. The nuclear modification factors for J/ψ production in SeaQuest as a function of x_F for pQCD production alone for (a) carbon, (b) iron, and (c) tungsten targets relative to deuterium. Results are shown for nPDF effects alone (red), nPDFs with an additional k_T kick (magenta), nPDFs and absorption (blue), and nPDFs, absorption and k_T broadening (cyan). The solid lines shown the results with the central EPPS16 set while the dashed curves denote the limits of adding the EPPS16 uncertainties in quadrature.

are outlined by the dashed curves. First nPDF effects alone are shown by the red points and curves. In this case, $g_A(k_T) = g_p(k_T)$, no additional broadening is taken into account due to the nuclear target. The magenta points and curves show the effect of enhanced k_T broadening in the nuclear target. Next, absorption is added in the two cases with nPDF effects plus absorption shown in the blue points and curves while all three effects: nPDF, absorption, and enhanced k_T broadening are shown by the cyan points and curves.

The results with nPDF effects alone are generally independent of x_F and p_T and all show $R_{pA} > 1$. As seen in Fig. 3, the x_F and p_T acceptance of the SeaQuest experiment restricts the x_2 range in the nuclear targets to a rather narrow window close to $x_2 \approx 0.1$ where antishadowing is dominant. The low scale of the calculation, not much greater than the minimum scale of EPPS16, indicates that the uncertainties will be larger than at higher scales. The EPPS16 nPDF uncertainties are large. The effects grow in magnitude as the target mass is increased from $A = 12$ to $A = 184$, as do the widths of the uncertainty bands. It is worth noting that only the lower limit of EPPS16 band gives $R_{pA} < 1$ in this case.

The effect of k_T broadening in the nucleus relative to the deuteron changes the shape of the p_T distribution, particularly at low p_T. By adding the δk_T^2 due to multiple scattering to the intrinsic k_T needed for J/ψ production in $p + p$ collisions, the

average p_T is increased in $p + A$ collisions. The tails of the p_T distributions are typically less affected, particularly at collider energies where the enhanced k_T broadening in a nuclear has to be large to produce a substantial effect because the added δk_T^2 is small compared with $\langle p_T \rangle$ of the J/ψ. In addition, if $\langle k_T^2 \rangle_A^{1/2}$ is much less than the mass of the particle to which it is applied the effect is reduced. For example, the effect of k_T broadening, even in $p + p$, is much smaller for bottom quarks than for charm quarks, see Refs. [82,83].

Because the mass scale of the J/ψ is larger than the applied k_T kick, the low center-of-mass energy of the SeaQuest experiment results in a larger effect than at collider energies and even than at other fixed-target energies. This effect is particularly visible on the p_T dependence of the suppression factor shown in Fig. 6. The broadening results in a substantial increase in R_{pA} with p_T, especially for heavier targets where δk_T^2 is a factor of 2 to 3 larger than the change in carbon.

It is notable, however, that there is also a slight change in the x_F dependence of R_{pA} due to broadening since $x_F = 2m_T \sinh y / \sqrt{s_{NN}}$. This change is significantly smaller than as a function of p_T because x_F depends instead on $m_T = (m^2 + p_T^2)^{1/2}$ and m and p_T are of comparable magnitude over the measured p_T range. Finally, there would be no change due to k_T broadening if the results were given as a function of rapidity instead.
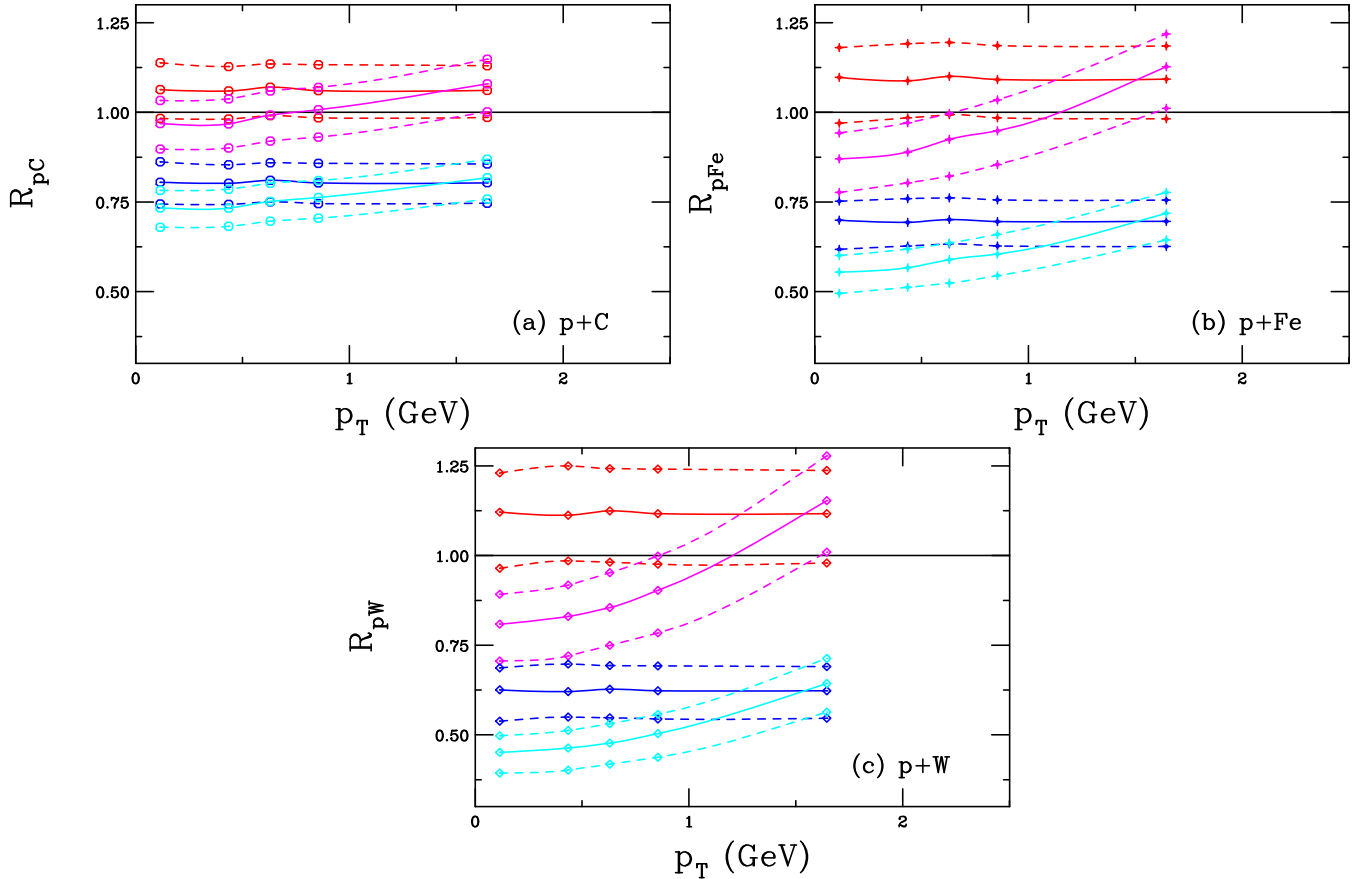
FIG. 6. The nuclear modification factors for J/ψ production in SeaQuest as a function of p_T for pQCD production alone for (a) carbon, (b) iron, and (c) tungsten targets relative to deuterium. Results are shown for EPPS16 nPDFs alone (red), EPPS16 with an additional k_T kick (magenta), nPDFs with absorption (blue), and nPDFs, absorption and k_T broadening (cyan). The solid lines show the results with the central EPPS16 set while the dashed curves denote the limits of adding the EPPS16 uncertainties in quadrature.

Rather strong absorption is required to nullify the effects of antishadowing and produce $R_{pA} < 1$, as seen when absorption is added to the calculation. Since a constant 9 mb cross section has been assumed, as inferred for midrapidity ($x_F \approx 0$) in Ref. [54], absorption does not change the dependence of R_{pA} on x_F and p_T. The effective exponent α obtained with $\sigma_{\rm abs} = 9$ mb is 0.88.

Reference [54] also showed that $\sigma_{\rm abs}$ could increase significantly with x_F for $x_F > 0.25$, resulting in a decrease of R_{pA} with x_F. In that reference and in other works (see, for example, Refs. [28,30,32,84]), the decrease with x_F was associated with energy loss, either in the initial state or in the final state. Here it is argued that this behavior could be attributed to intrinsic charm. This possibility will be tested in the next section where the effects on an intrinsic charm contribution is studied.

In Ref. [54], away from midrapidity but for $x_F \leqslant 0.25$, the effective absorption cross section could be interpreted as starting to decrease with x_F, especially for higher fixed-target energies. This could be attributed, for example, to the J/ψ being formed outside the target. Given the forward acceptance of the SeaQuest experiment, well forward of the acceptances of most of the experiments included in Ref. [54], it is possible that a lower value of $\sigma_{\rm abs}$ could be extracted from comparison with the SeaQuest data.

B. R_{pA} including intrinsic charm

Intrinsic charm is added to the calculations of R_{pA} here. In this case,

$$\sigma_{pA} = \sigma_{\rm CEM}(pA) + \sigma_{\rm ic}^{J/\psi}(pA), \tag{27}$$

$$\sigma_{pd} = 2\sigma_{\rm CEM}(pp) + \sigma_{\rm ic}^{J/\psi}(pA). \tag{28}$$

Here $\sigma_{\rm CEM}(pA)$ was defined in Eq. (23) while $\sigma_{\rm ic}^{J/\psi}(pA)$ is given in Eq. (21). Note that, unlike the nuclear volume-like mass dependence of the perturbative QCD effects, the nuclear surface-like A dependence is assumed to apply to the deuteron. Later in this section, this assumption will be relaxed to check the dependence of the results on this assumption. Three values of $P_{\rm ic5}^0$ in Eq. (18) are shown in the following four figures: 0.1%, 0.31%, and 1%. This range can be taken as an uncertainty band on intrinsic charm.

As in the previous section, the effects are added sequentially in these figures. Now nPDF effects and intrinsic charm are common to all the calculated ratios. The EPPS16 results are presented with the central best-fit set given by the solid curves while the uncertainties added in quadrature are outlined by the dashed curves. Those calculations, affecting $\sigma_{\rm CEM}$, are added to the intrinsic charm cross section, as in
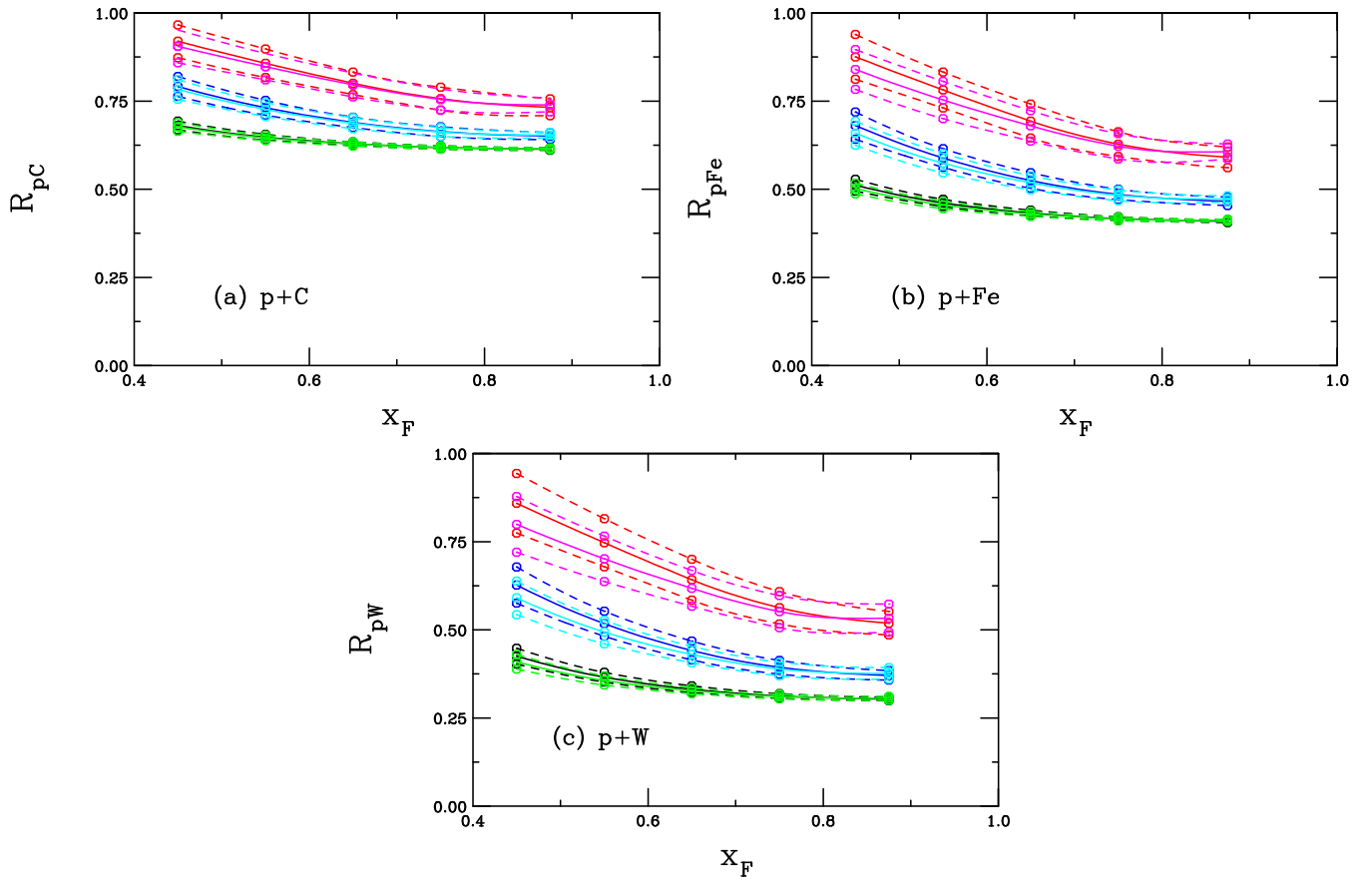
FIG. 7. The nuclear modification factors for J/ψ production in SeaQuest as a function of x_F for the combined pQCD and intrinsic charm cross section ratios for (a) carbon, (b) iron and (c) tungsten targets relative to deuterium. All calculations are shown with $\sigma_{abs} = 0$. Results with nPDF effects and the same k_T in $p + $d and $p + A$ are shown in the red, blue, and black curves while nPDF effects with an enhanced k_T kick in the nucleus are shown in the magenta, cyan, and green curves. The probability for IC production is 0.1% in the red and magenta curves; 0.31% in the blue and cyan curves; and 1% in the black and green curves. The solid lines show the results with the central EPPS16 set while the dashed curves denote the limits of adding the EPPS16 uncertainties in quadrature.

Eqs. (27) and (28). Results are shown without absorption, $\sigma_{abs} = 0$, in Figs. 7 and 8 while absorption is included with $\sigma_{abs} = 9$ mb in Figs. 9 and 10.

In these figures, the red, blue, and black curves show the nPDF effects with $P_{ic5}^0 = 0.1\%$, 0.31%, and 1% respectively in Figs. 7 and 8. The solid curves show the EPPS16 central value while the dashed curves outline the uncertainty band. For these calculations, $g_A(k_T) = g_p(k_T)$. The magenta, cyan and green solid and dashed curves include enhanced k_T broadening in the nuclear target for $P_{ic5}^0 = 0.1\%$, 0.31%, and 1% respectively. The same color scheme is used in Figs. 9 and 10 but with absorption included in $\sigma_{CEM}(pA)$.

The nuclear dependence of intrinsic charm is not shown separately because no other nuclear effects are active with this component, only the A^β dependence shown in Eq. (21). Thus R_{pA} for intrinsic charm alone would be independent of x_F and p_T. Since intrinsic charm is included only in the initial proton and the J/ψ comes on shell without a hard interaction with the target, there are no nPDF effects. For the same reason, the intrinsic charm contribution is unaffected by multiple scattering of the proton in the target nucleus.

The effect of the intrinsic charm contribution is immediately clear in Fig. 7: $R_{pA} < 1$ without nuclear absorption and is now a decreasing function of x_F. It is also clear that, at least for the SeaQuest energy and in its forward acceptance, the intrinsic charm cross section is comparable to the perturbative QCD cross section. As P_{ic5}^0 increases from 0.1% to 1%, the intrinsic charm contribution comes to dominate the nuclear dependence as a function of x_F. The most immediate qualitative measure of this dominance is apparent in the width of the EPPS16 uncertainty band. These bands are wide in Figs. 5 and 6 without intrinsic charm, narrower but still relatively far apart for $P_{ic5}^0 = 0.1\%$, and barely distinguishable for $P_{ic5}^0 = 1\%$ because, in this case, the nuclear dependence is wholly dominated by intrinsic charm.

There is some notable separation between the different assumed values of P_{ic5}^0 without absorption included. The difference due to the k_T broadening, apparent for the red and magenta curves in Fig. 7, especially for the iron and tungsten targets, is almost indistinguishable for $P_{ic}^0 = 1\%$, in the black and green curves. The dominance of the intrinsic charm contribution as P_{ic5}^0 increases also becomes obvious in the weakening of the x_F dependence with increasing P_{ic5}^0. When a
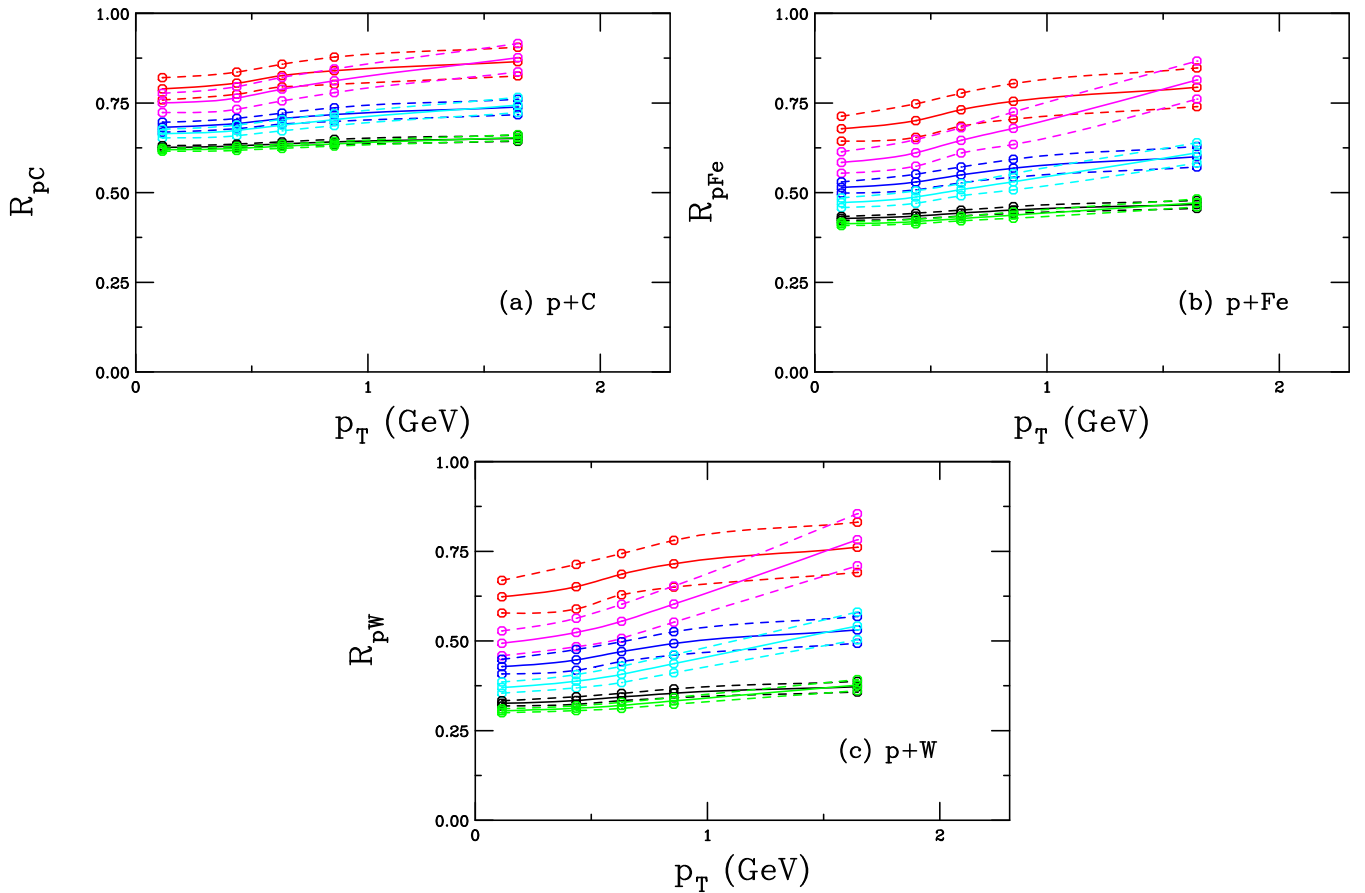
FIG. 8. The nuclear modification factors for J/ψ production in SeaQuest as a function of p_T for the combined pQCD and intrinsic charm cross section ratios for (a) carbon, (b) iron, and (c) tungsten targets relative to deuterium. All calculations are shown with $\sigma_{abs} = 0$. Results with nPDF effects and the same k_T in $p + d$ and $p + A$ are shown in the red, blue, and black curves while nPDFs with an enhanced k_T kick in the nucleus are shown in the magenta, cyan, and green curves. The probability for IC production is 0.1% in the red and magenta curves; 0.31% in the blue and cyan curves; and 1% in the black and green curves. The solid lines shown the results with the central EPPS16 set while the dashed curves denote the limits of adding the EPPS16 uncertainties in quadrature.

1% probability is assumed, the results are almost independent of x_F except in the lowest x_F bins, as would be expected if J/ψ production was via the intrinsic charm contribution alone.

Similar behavior is observed as a function of p_T in Fig. 8. Even without an enhanced k_T broadening in the nucleus, a rise in R_{pA} with p_T is still observed, although it is not as strong a function of p_T without broadening as it is with it. In this case, with the same k_T kick in $p + A$ as in $p + p$, there is an increase compared with $p_T \rightarrow 0$ which then levels off in the last two, larger p_T, bins. On the other hand, when broadening is included, the rise in R_{pA} with p_T continues over the entire p_T range shown. The perturbative QCD and intrinsic charm contributions are thus competitive with each other as long as P^0_{ic5} is low, 0.31% or less, but not for $P^0_{ic5} = 1\%$ where the distinction between calculations with and without broadening is negligible.

Results including absorption are given in Figs. 9 and 10. The strong absorption cross section employed in these calculations, $\sigma_{abs} = 9$ mb, results in dominance of the intrinsic charm contribution even when P^0_{ic5} is as low as 0.1%. Note, however, that the dependence of R_{pA} with x_F and p_T is not significantly affected by an assumed 1% probability for

intrinsic charm because, for this value of P^0_{ic5}, the intrinsic charm contribution is already dominant with $\sigma_{abs} = 0$, the higher probability overcomes the stronger surface nuclear target dependence of intrinsic charm. Now, with absorption included, the A dependence of the two contributions are similar in magnitude since $S_A^{abs} \approx A^\alpha = A^{0.88}$, see the discussion under Eq. (12) in Sec. II C. Even though α is still greater than $\beta = 0.71$, assumed for intrinsic charm [1,31], the two values are more comparable.

The calculations including absorption further compresses the pQCD uncertainties due to nPDF effects and k_T broadening. The differences between the calculations with nPDF effects only and nPDFs with k_T broadening on the perturbative part are almost indistinguishable as a function of x_F except for the heaviest targets, as seen in Fig. 9. The same can be seen as a function of p_T in Fig. 10. In this figure, the differences between the results without and with k_T broadening are only visible for $P^0_{ic5} = 0.1\%$.

The assumptions made about how intrinsic charm is implemented are now tested. First, the assumption regarding whether one treats the deuterium target as a nucleus or like a proton is tested, with results shown in Fig. 11. Next, the
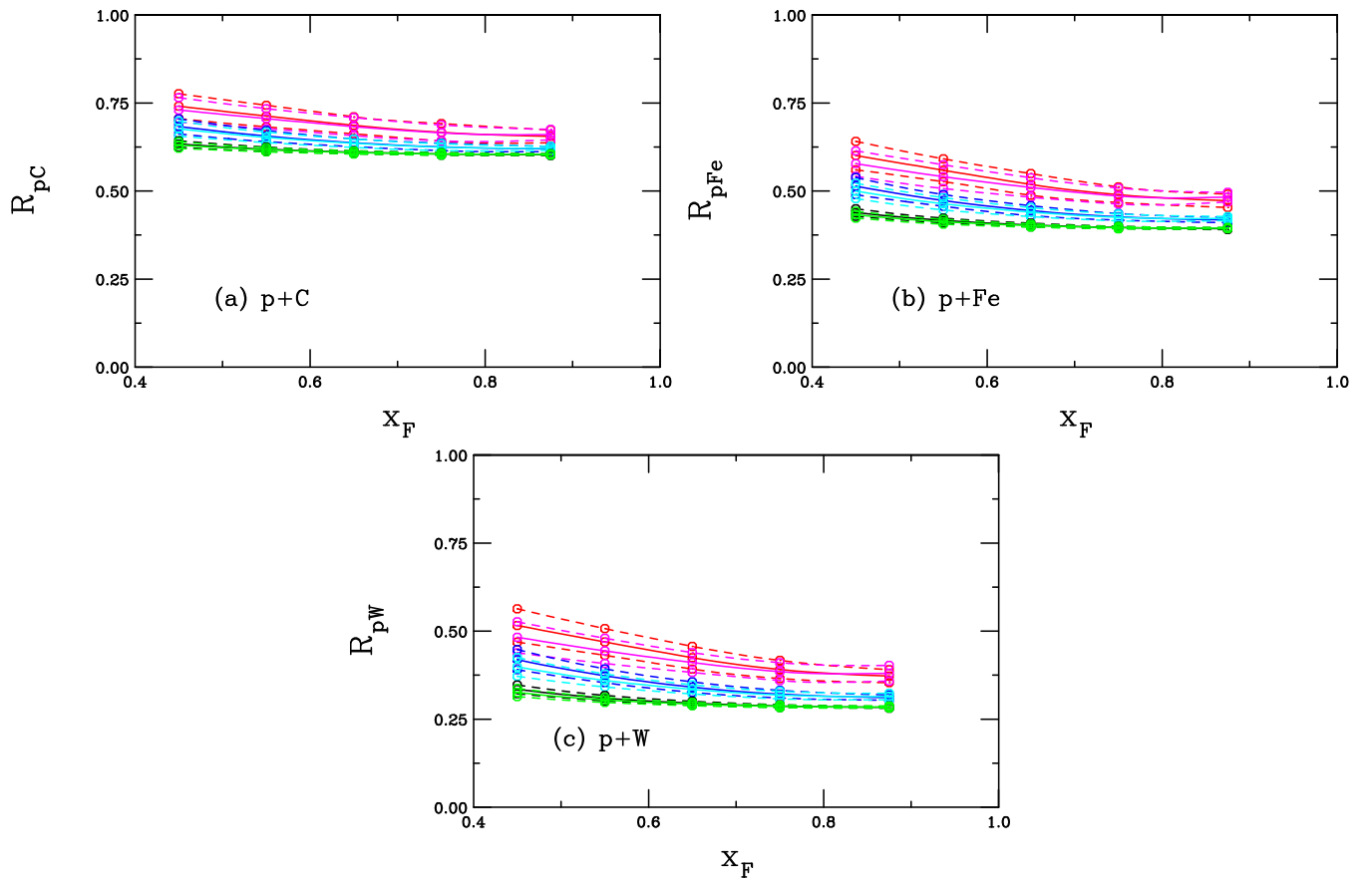
FIG. 9. The nuclear modification factors for J/ψ production in SeaQuest as a function of x_F for the combined pQCD and intrinsic charm cross section ratios for (a) carbon, (b) iron, and (c) tungsten targets relative to deuterium. All calculations are shown with nuclear absorption included. Results with EPPS16 and the same k_T in $p+d$ and $p+A$ are shown in the red, blue, and black curves while EPPS16 with an enhanced k_T kick in the nucleus are shown in the magenta, cyan, and green curves. The probability for IC production is 0.1% in the red and magenta curves; 0.31% in the blue and cyan curves; and 1% in the black and green curves. The solid lines shown the results with the central EPPS16 set while the dashed curves denote the limits of adding the EPPS16 uncertainties in quadrature.

influence of the range of k_T integration on the intrinsic charm p_T distribution is checked in Fig. 12.

When calculating R_{pA} with a deuteron target, it has so far been assumed that the surface-like A dependence also applies to the deuteron, unlike the assumption that $\sigma_{abs} = 0$, a pure volume-like A dependence, for perturbative QCD effects. This has the effect of reducing the intrinsic charm contribution in $p+d$ interactions relative to $p+A$ for heavier nuclei. In Fig. 11, it is assumed that, also in the case of intrinsic charm, the deuteron target is effectively the same as a proton target, with $\beta = 1$ in Eq. (21). Instead of showing all values of P^0_{ic5}, only calculations with $P^0_{ic5} = 0.31\%$ are presented.

Results are given for all three targets with EPPS16 and absorption. Calculations both with and without an intrinsic k_T enhancement are presented. The R_{pA} ratios are, from top to bottom, $p+C$ (red without k_T enhancement and magenta with); $p+Fe$ (blue and cyan); and $p+W$ (black and green). Making the intrinsic charm contribution in $p+d$ the same as in $p+p$ has the effect of reducing the magnitude of the ratios by a few percent without changing the shape of R_{pA} as a function of x_F or p_T. The difference would be slightly larger for a smaller value of P^0_{ic5} but would not change the overall

result significantly. Thus, at least from the point of view of statistics with a proton or deuteron target, there is no reason, calculationally, to prefer one over the other.

To end the discussion of the SeaQuest predictions in this section, Fig. 12 shows how R_{pA} could be modified as a function of p_T if a wider range of k_T integration for intrinsic charm had been chosen. In particular, $k_q^{max} = 0.4$ GeV and $k_c^{max} = 2$ GeV are assumed since this choice resulted in a broader J/ψ distribution from intrinsic charm with a correspondingly reduced peak of the p_T distribution at low p_T, in the range of the SeaQuest acceptance. Results are not also shown for the lower values because, although the p_T distribution becomes somewhat narrower, the effect is not large enough to modify the results. The nuclear suppression factor is only shown as a function of p_T because the range of k_T integration has no effect on the x_F distribution of the produced J/ψ, see Fig. 4.

Similar to the results shown in Fig. 11, only $P^0_{ic5} = 0.31\%$ is presented for all three targets, without and with enhanced k_T broadening, in addition to nPDF effects and absorption. The broader intrinsic charm p_T distribution does not change the overall suppression of R_{pA} significantly but it does show
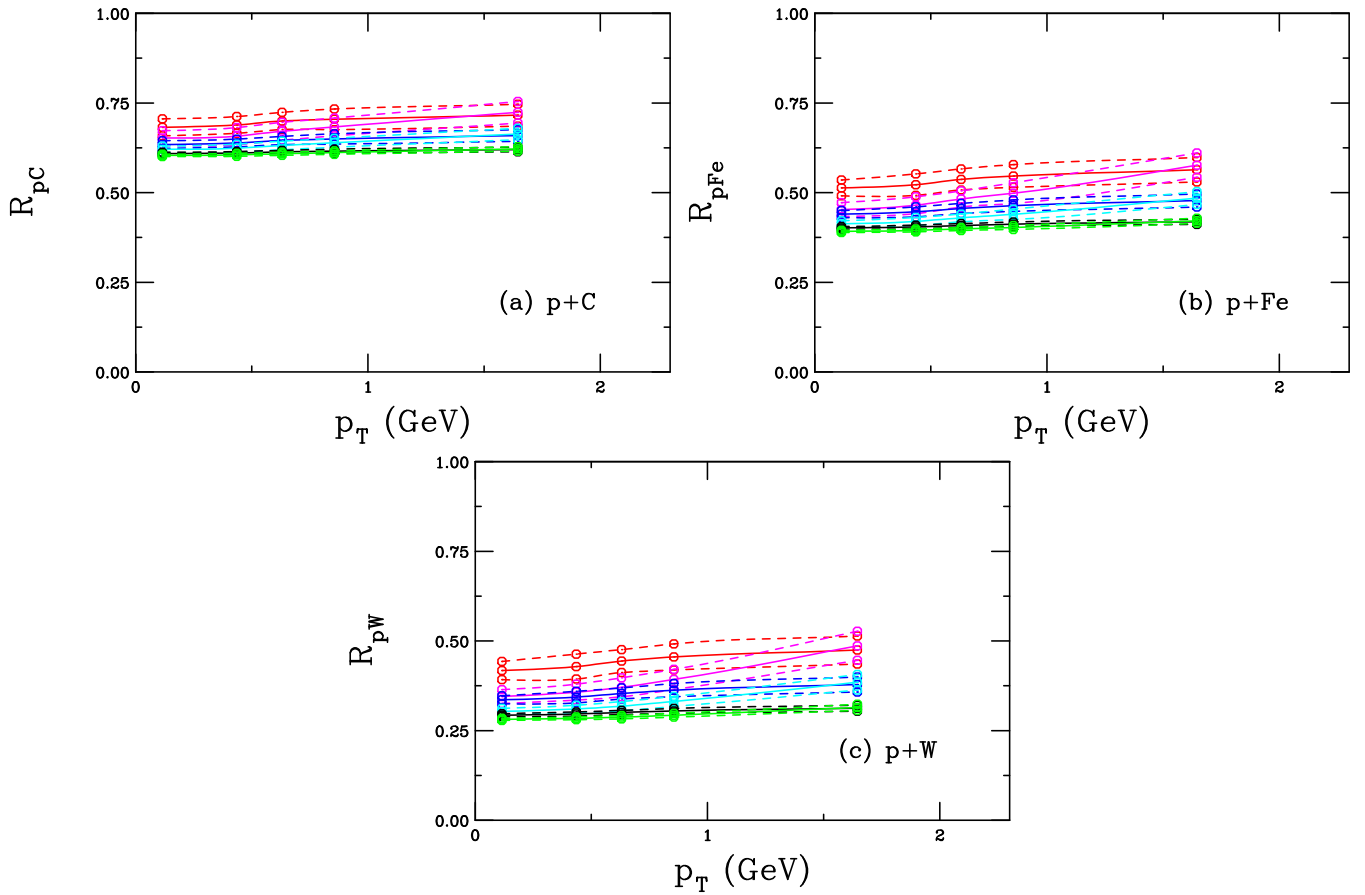
FIG. 10. The nuclear modification factors for J/ψ production in SeaQuest as a function of pT for the combined pQCD and intrinsic charm cross section ratios for (a) carbon, (b) iron, and tungsten targets relative to deuterium. All calculations are shown with nuclear absorption included. Results with EPPS16 and the same k_T in $p + $ d and $p + A$ are shown in the red, blue, and black curves while EPPS16 with an enhanced k_T kick in the nucleus are shown in the magenta, cyan, and green curves. The probability for IC production is 0.1% in the red and magenta curves; 0.31% in the blue and cyan curves; and 1% in the black and green curves. The solid lines shown the results with the central EPPS16 set while the dashed curves denote the limits of adding the EPPS16 uncertainties in quadrature.
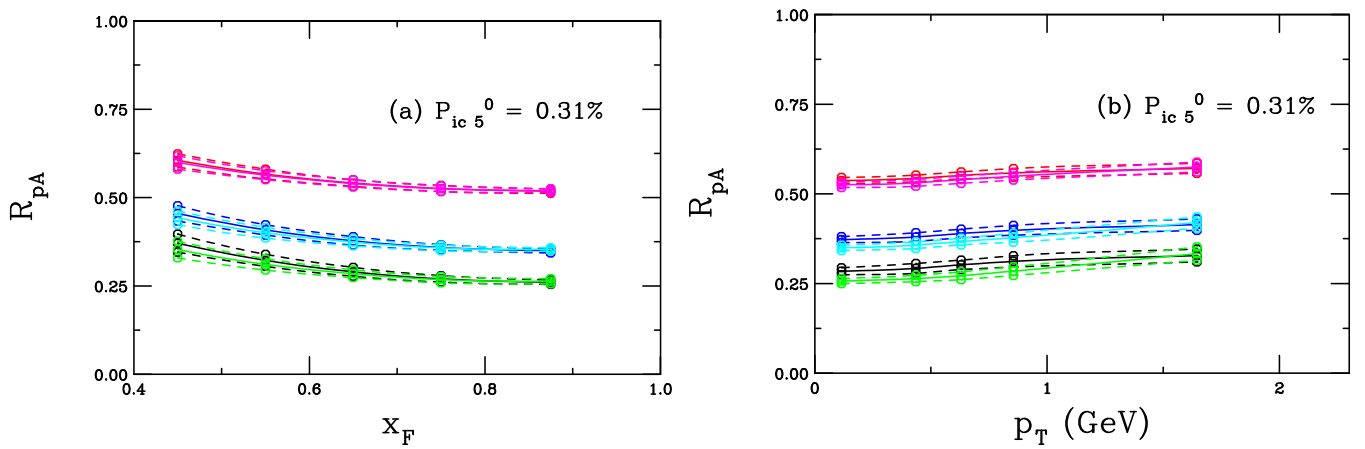

FIG. 11. The nuclear modification factors for J/ψ production in SeaQuest as a function of (a) x_F and (b) p_T for the combined pQCD and intrinsic charm cross section ratios for carbon (red and magenta curves), iron (blue and cyan curves), and tungsten (black and green curves) targets relative to a proton target. All calculations are shown with nuclear absorption included. Results with EPPS16 and the same k_T in $p + p$ and $p + A$ are shown in the red, blue, and black curves while EPPS16 with an enhanced k_T kick in the nucleus are shown in the magenta, cyan, and green curves. The probability for IC production is 0.31% in all cases. The solid lines shown the results with the central EPPS16 set while the dashed curves denote the limits of adding the EPPS16 uncertainties in quadrature.
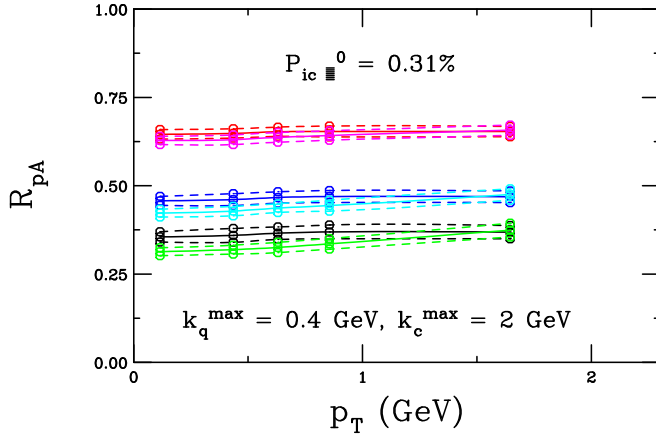
FIG. 12. The nuclear modification factors for J/ψ production in SeaQuest as a function of p_T for the combined pQCD and intrinsic charm cross section ratios for carbon (red and magenta curves), iron (blue and cyan curves), and tungsten (black and green curves) targets relative to a proton target. All calculations are shown with nuclear absorption included. Results with EPPS16 and the same k_T in $p + d$ and $p + A$ are shown in the red, blue, and black curves while EPPS16 with an enhanced k_T kick in the nucleus are shown in the magenta, cyan, and green curves. The probability for IC production is 0.31% in all cases. A broader IC distribution is assumed here, corresponding to the blue dashed curve in Fig. 4(b). The solid lines shown the results with the central EPPS16 set while the dashed curves denote the limits of adding the EPPS16 uncertainties in quadrature.

a larger difference between calculations with additional k_T broadening and those without.

C. Comparison with E866 data

Here data for the exponent α in Eq. (1), obtained by the E866 Collaboration, are compared with a subset of the calculations shown previously. The previous part of this section added cold nuclear matter effects systematically. In this part, only calculations with absorption and k_T broadening are shown. The absorption calculation employs $\sigma_{abs} = 5$ mb, in accord with the energy dependence of σ_{abs} described in Ref. [54]. The default k_T kick, with more broadening in the nucleus than in the proton, is included. Only results for the central EPPS16 set are presented. The variation of the results without and with intrinsic charm are instead highlighted. First α is given without intrinsic charm and subsequently $P_{ic5}^0 = 0.1\%$, 0.31%, and 1% are employed.

The value of α as a function of x_F is shown in Fig. 13(a) while the dependence of α on p_T in the three x_F regions employed by the E866 collaboration are given in Figs. 13(b)–13(d). The calculations are averaged over all three nuclear targets.

The agreement with $\alpha(x_F)$ measured by E866 is quite good, especially for $P_{ic5}^0 = 1\%$ which produces a somewhat stronger dependence of α on x_F than required. Results without intrinsic charm are almost independent of x_F, clearly in disagreement with the trend of the data. The calculations with a finite intrinsic charm contribution do not begin to diverge from that with $P_{ic5}^0 = 0$ until $x_F > 0.25$, where the intrinsic

charm probability distribution begins to rise above that of the perturbative QCD result which decreases as the gluon distribution falls steeply at large x of the projectile. This can be seen in Fig. 14(a) which shows the calculated x_F distributions in $p + p$ collisions. As the intrinsic charm probability grows, the intermediate to large x_F contribution grows above the pQCD contribution, resulting in a shoulder-like structure for the 1% probability until $x_F > 0.75$. However, as $x_F \to 1$, the intrinsic charm contribution to the cross section falls steeply until it approaches the pQCD contribution once more, causing the rise of α toward unity for $x_F > 0.88$. Clearly, if the intrinsic charm contribution to the cross section effectively vanishes, the nuclear dependence of the pQCD contribution will dominate, resulting in the rise of $\alpha(x_F)$ at high x_F.

The agreement of the calculated $\alpha(p_T)$ with the data is also generally very good except that, now, the lower intrinsic charm probabilities agree best with the data, particularly for $p_T > 3$ GeV, near the end of the measured p_T range. The difference in the results becomes more pronounced for the higher-x_F ranges, especially for the high-x_F data set. This is not surprising when one looks at the x_F distributions in Fig. 14(a). In the low x_F region, $-0.1 < x_F < 0.3$, integrated over all p_T, only $P_{ic5}^0 = 1\%$ shows significant deviation from the perturbative QCD x_F distribution for the proton. However, recalling the harder intrinsic charm J/ψ p_T distribution, integrated over all x_F in Fig. 4(b), at sufficiently high p_T, the intrinsic charm contribution will begin to dominate, even in the low-x_F region. As the x_F range covered becomes larger, from the intermediate-x_F to the high-x_F regions, the intrinsic charm contribution dominates the x_F range and the shape of $\alpha(p_T)$ is defined by the A dependence of the intrinsic charm contribution. The p_T distributions from both perturbative QCD and intrinsic charm are shown in Figs. 14(b)–14(d). In the high-x_F bin in particular, a separation can be seen between the distributions including intrinsic charm from that without it, even for low values of P_{ic5}^0 and low p_T. These distributions show that, in the SeaQuest x_F range, intrinsic charm dominates the p_T dependence over the entire x_F acceptance region.

It is notable that $\alpha(p_T)$ begins to turn over and decrease at high p_T, even in the low-x_F region. Here, where the J/ψ p_T distribution is dominated by intrinsic charm, one can expect that α should asymptotically match the A dependence of intrinsic charm, $A^{0.71}$. Indeed, in the high-x_F bin and $P_{ic5}^0 = 1\%$, one sees that $\alpha(p_T) \to 0.71$.

Clearly, a larger intrinsic charm probability does not match the E866 data at high p_T. However, the overall trend is generally very good for this default calculation. No tuning of the calculation has been done to match the data, only the energy dependence of the model ingredients has been taken into account. In addition, no uncertainties are shown for the EPPS16 nuclear modifications and these can be significant, as seen in the SeaQuest results. There does appear to be tension between the results for $\alpha(x_F)$ and $\alpha(p_T)$ because $\alpha(x_F)$ would prefer a higher value of P_{ic5}^0 while $\alpha(p_T)$ prefers a smaller intrinsic charm probability. However, the p_T dependence of intrinsic charm has not been as thoroughly explored. As noted in Sec. III and in Fig. 12 above, the shape of the intrinsic charm p_T distribution depends on the integration range of
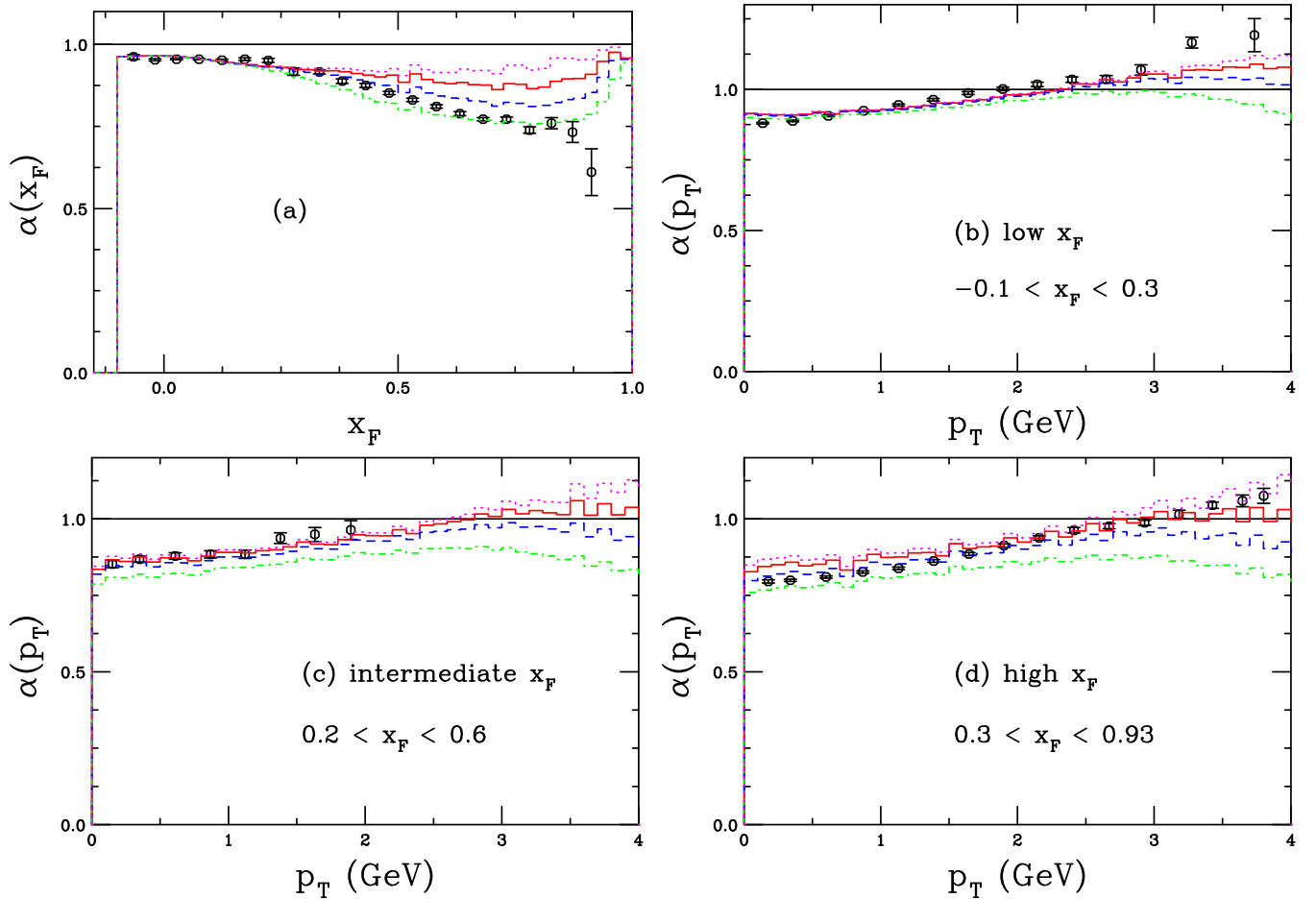
FIG. 13. The exponent α as a function of (a) x_F and as a function of p_T for the (b) low-x_F, (c) intermediate-x_F, and (d) high-x_F regions. The dotted magenta curves are without intrinsic charm while the solid red, dashed blue, and dot-dashed green curves employ $P_{\mathrm{ic5}}^0 = 0.1\%$, 0.31%, and 1% respectively. The E866 data [6] are shown by the black points.

the internal transverse momentum and on the values of the quark masses employed. Either employing a narrower k_q and k_c integration range or choosing to use current quark masses for the light quarks can produce in a steeper J/ψ intrinsic charm p_T distribution, improving the agreement with the data at high p_T.

As the energy is increased further, the pQCD contribution to the total cross section from both components will grow faster with energy than the intrinsic charm contribution which only increases with energy based on the growth of the inelastic $p + p$ cross section. Between the E866 energy and $\sqrt{s_{NN}} = 200$ GeV at RHIC, $\sigma_{pp}^{\mathrm{in}}$ increases by $\approx 30\%$ while the J/ψ production cross section grows by more than an order of magnitude [39]. In addition, the high-x_F region is not well covered by collider detectors, making the intrinsic charm signal harder to detect at colliders.

V. CONCLUSIONS

The low center-of-mass energy of the SeaQuest experiment, as well as its forward acceptance, make it an ideal environment for probing the existence of an intrinsic charm contribution to J/ψ production. The center-of-mass energy is

a factor of 3.1 above the J/ψ production threshold. This relatively low energy makes the perturbative QCD cross section compatible with or less than the J/ψ cross section from intrinsic charm, depending on the experimental x_F range. Higher center-of-mass energies increase the J/ψ cross section in the CEM dramatically, see, e.g., Ref. [39], while the intrinsic charm contribution grows more slowly, depending only on $\sigma_{pN}^{\mathrm{in}}$, see Eq. (19). In addition, the high-x_F range covered by SeaQuest is exactly the region where intrinsic charm should dominate production. As seen in a comparison of the x_F distributions in Figs. 1(a) and 4(a), the CEM cross section decreases by an order of magnitude over the SeaQuest x_F acceptance, with a maximum at $x_F = 0$, outside the SeaQuest acceptance. On the other hand, the peak of intrinsic charm probability distribution is at $x_F \approx 0.53$, within the range of the SeaQuest measurement.

The comparison with the higher energy E866 J/ψ nuclear dependence shows that the model described here is generally consistent with the existing data, especially when intrinsic charm is included. Some uncertainties still remain and the model could be further refined. it is clear, however, that higher energies will further reduce the potential for seeing an intrinsic charm signal, especially if the detector setups
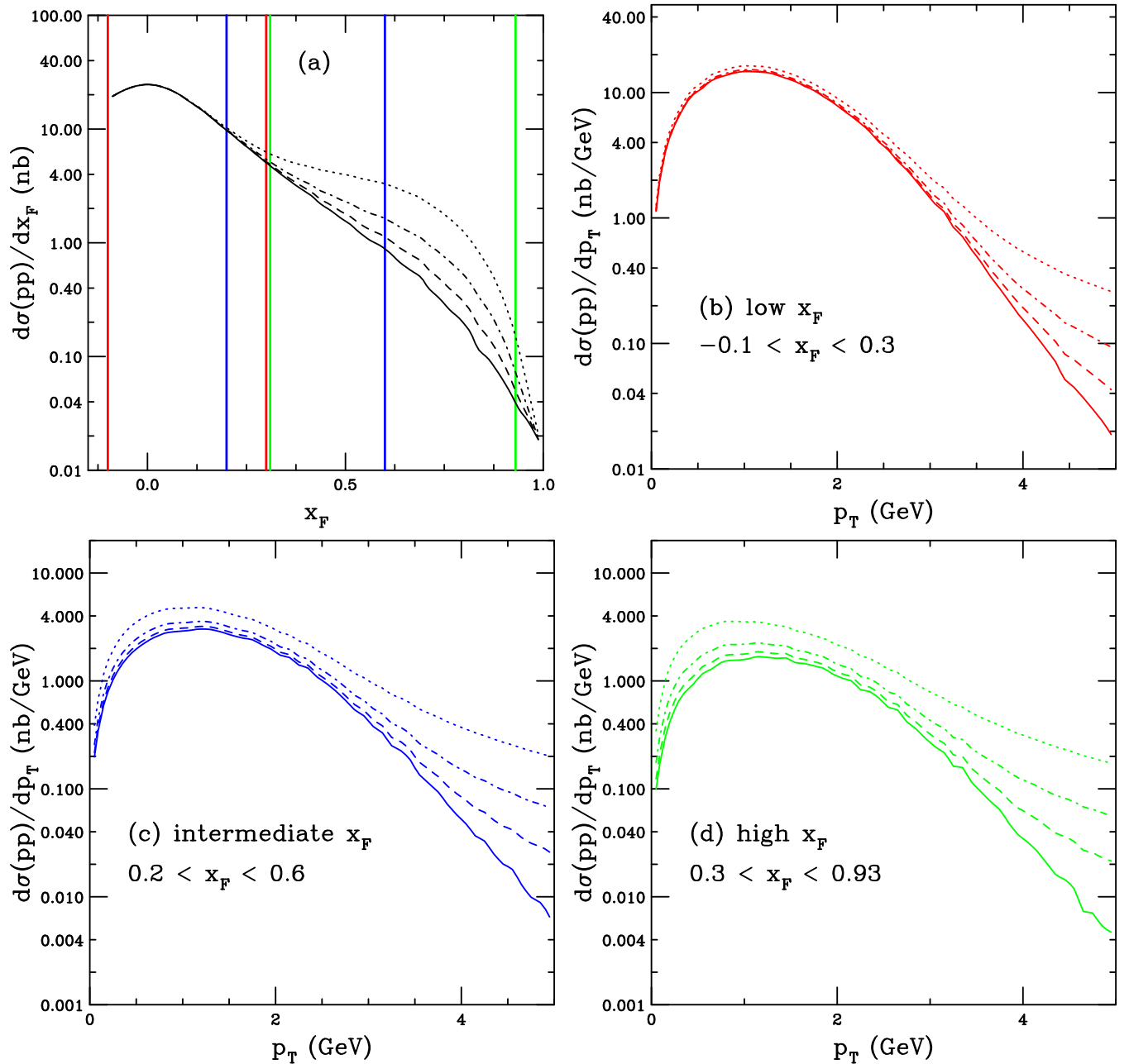
FIG. 14. The J/ψ cross sections in $p + p$ collisions at $\sqrt{s} = 38.8$ GeV with and without an intrinsic charm contribution as a function of (a) x_F and p_T at (b) low-x_F, (c) intermediate-x_F, and (d) high-x_F. The solid curves do not include intrinsic charm while the dashed, dot-dashed, and dotted curves are calculated with $P_{ic5}^0 = 0.1\%$, 0.31%, and 1%, respectively. The vertical bars on the x_F distributions show the upper and lower limits of the x_F ranges for the corresponding p_T distributions shown in panels (b)–(d). The color of the bars matches the color of the curves in panels (b)–(d).

do not cover sufficiently high x_F. Fixed-target kinematics are thus preferable for the discovery potential of intrinsic charm.

A comparison of the SeaQuest J/ψ production data on its nuclear targets, once available, could set limits on σ_{abs} in the perturbative QCD contribution and P_{ic5}^0, the probability of the intrinsic charm contribution in the proton. A high statistics measurement of the p_T dependence could determine the transverse momentum spread of the partons in the proton as well as the allowed parton masses; that is, whether the

distributions are more compatible with constituent or current quark masses.

[1] J. Badier *et al.* (NA3 Collaboration), Experimental J/ψ hadronic production from 150 GeV/c to 280 GeV/c, Z. Phys. C: Part. Fields **20**, 101 (1983).

[2] S. Katsanevas, C. Kourkoumelis, A. Markou, L. K. Resvanis, S. Tzamarias, G. Voulgaris *et al.* (E537 Collaboration), Nuclear Target Effects in J/ψ Production in 125 GeV/c Antiproton and π^- Interactions, Phys. Rev. Lett. **60**, 2121 (1988).

[3] D. M. Alde, H. W. Baer, T. A. Carey, G. T. Garvey, A. Klein, C. Lee *et al.* (E772 Collaboration), The A Dependence of J/ψ and ψ' Production at 800 GeV/c, Phys. Rev. Lett. **66**, 133 (1991).

[4] M. H. Schub, D. M. Jansen, C. S. Mishra, P. M. Ho, C. N. Brown, T. A. Carey *et al.* (E789 Collaboration), Measurement of J/ψ and ψ' production in 800 GeV/c proton - gold collisions, Phys. Rev. D **52**, 1307 (1995); Measurement of J/ψ and ψ' production in 800 GeV/c proton - gold collisions, **53**, 570(E) (1996).

[5] B. Alessandro *et al.* (NA50 Collaboration), Charmonium production and nuclear absorption in pA interactions at 450 gev, Eur. Phys. J. C **33**, 31 (2004).

[6] M. J. Leitch, W. M. Lee, M. E. Beddo, C. N. Brown, T. A. Carey, T. H. Chang *et al.* (NuSea Collaboration), Measurement of Differences between J/ψ and ψ' Suppression in p–A Collisions, Phys. Rev. Lett. **84**, 3256 (2000).

[7] I. Abt *et al.* (HERA-B Collaboration), Measurement of the J/ψ production cross section in 920GeV/c fixed-target proton-nucleus interactions, Phys. Lett. B **638**, 407 (2006).

[8] I. Abt *et al.* (HERA-B Collaboration), Kinematic distributions and nuclear effects of J/ψ production in 920 GeV fixed-target proton-nucleus collisions, Eur. Phys. J. C **60**, 525 (2009).

[9] A. Adare *et al.* (PHENIX Collaboration), Nuclear Modification of ψ', χ_c, and J/ψ Production in d + Au Collisions at $\sqrt{s_{NN}} =$ 200 GeV, Phys. Rev. Lett. **111**, 202301 (2013).

[10] L. Adamczyk *et al.* (STAR Collaboration), J/ψ production at low transverse momentum in $p + p$ and d+Au collisions at $\sqrt{s_{NN}} = $ 200 GeV, Phys. Rev. C **93**, 064904 (2016).

[11] B. B. Abelev *et al.* (ALICE Collaboration), J/ψ production and nuclear effects in p-Pb collisions at $\sqrt{s_{NN}} = $ 5.02 TeV, J. High Energy Phys. 02 (2014) 073.

[12] R. Aaij *et al.* (LHCb Collaboration), Study of J/ψ production and cold nuclear matter effects in pPb collisions at $\sqrt{s_{NN}} = 5$ TeV, J. High Energy Phys. 02 (2014) 072.

[13] A. M. Sirunyan *et al.* (CMS Collaboration), Measurement of prompt and nonprompt J/ψ production in pp and pPb collisions at $\sqrt{s_{NN}} = $ 5.02 TeV, Eur. Phys. J. C **77**, 269 (2017).

[14] G. Aad *et al.* (ATLAS Collaboration), Measurement of differential J/ψ production cross sections and forward-backward ratios in p + Pb collisions with the ATLAS detector, Phys. Rev. C **92**, 034904 (2015).

[15] C. A. Aidala *et al.* (SeaQuest Collaboration), The SeaQuest Spectrometer at Fermilab, Nucl. Instrum. Methods Phys. Res., Sect. A **930**, 49 (2019).

[16] S. J. Brodsky, P. Hoyer, C. Peterson, and N. Sakai, The intrinsic charm of the proton, Phys. Lett. B **93**, 451 (1980).

[17] S. J. Brodsky, C. Peterson, and N. Sakai, Intrinsic heavy quark states, Phys. Rev. D **23**, 2745 (1981).

[18] S. J. Brodsky and P. Hoyer, The Nucleus as a Color Filter in QCD Decays: Hadroproduction in Nuclei, Phys. Rev. Lett. **63**, 1566 (1989).

[19] J. J. Aubert *et al.* (EMC Collaboration), An experimental limit on the intrinsic charm component of the nucleon, Phys. Lett. B **110**, 73 (1982).

[20] P. Chauvat *et al.* (R608 Collaboration), Production of Λ_c with Large x_F at the ISR, Phys. Lett. B **199**, 304 (1987).

[21] R. Vogt and S. J. Brodsky, Intrinsic charm production of doubly charmed baryons: Collider vs. fixed-target, Sci. China: Phys., Mech. Astron. **63**, 221066 (2020).

[22] M. Agnello *et al.* (NA60+ Collaboration), Study of hard and electromagnetic processes at CERN-SPS energies: An investigation of the high-$\mu_{\mathbf{B}}$ region of the QCD phase diagram with NA60+, arXiv:1812.07948.

[23] L. Massacrier, B. Trzeciak, F. Fleuret, C. Hadjidakis, D. Kikola, J. P. Lansberg, and H. S. Shao, Feasibility studies for quarkonium production at a fixed-target experiment using the LHC proton and lead beams (AFTER@LHC), Adv. High Energy Phys. **2015**, 986348 (2015).

[24] R. Aaij *et al.* (LHCb Collaboration), First Measurement of Charm Production in its Fixed-Target Configuration at the LHC, Phys. Rev. Lett. **122**, 132002 (2019).

[25] R. Vogt, J/ψ production and suppression, Phys. Rep. **310**, 197 (1999).

[26] D. Kharzeev, C. Lourenço, M. Nardi, and H. Satz, A quantitative analysis of charmonium suppression in nuclear collisions, Z. Phys. C: Part. Fields **74**, 307 (1997).

[27] M. Arneodo, Nuclear effects in structure functions, Phys. Rep. **240**, 301 (1994).

[28] S. Gavin and J. Milana, Energy Loss at Large x_F in Nuclear Collisions, Phys. Rev. Lett. **68**, 1834 (1992).

[29] S. J. Brodsky and P. Hoyer, A bound on the energy loss of partons in nuclei, Phys. Lett. B **298**, 165 (1993).

[30] F. Arleo and S. Peigne, J/ψ Suppression in p–A Collisions from Parton Energy Loss in Cold QCD Matter, Phys. Rev. Lett. **109**, 122301 (2012).

[31] R. Vogt, S. J. Brodsky, and P. Hoyer, Systematics of J/ψ production, Nucl. Phys. B **360**, 67 (1991).

[32] R. Vogt, The x_F dependence of ψ and Drell-Yan production, Phys. Rev. C **61**, 035203 (2000).

[33] C. Ayuso, Nuclear modification of J/Psi and Drell-Yan production at the E906/SeaQuest experiment, Ph.D. thesis, University of Michigan, 2020, doi:10.2172/1637630.

[34] R. Gavai, D. Kharzeev, H. Satz, G. A. Schuler, K. Sridhar, and R. Vogt, Quarkonium production in hadronic collisions, Int. J. Mod. Phys. A **10**, 3043 (1995).

[35] G. T. Bodwin, E. Braaten, and G. P. Lepage, Rigorous QCD analysis of inclusive annihilation and production of heavy quarkonium, Phys. Rev. D **51**, 1125 (1995).

[36] Y. Q. Ma and R. Vogt, Quarkonium production in an improved color evaporation model, Phys. Rev. D **94**, 114029 (2016).

[37] N. Brambilla, S. Eidelman, B. K. Heltsley, R. Vogt, G. T. Bodwin, E. Eichten *et al.*, Heavy quarkonium: Progress, puzzles, and opportunities, Eur. Phys. J. C **71**, 1534 (2011).

[38] H. L. Lai, M. Guzzi, J. Huston, Z. Li, P. M. Nadolsky, J. Pumplin, and C. P. Yuan, New parton distributions for collider physics, Phys. Rev. D **82**, 074024 (2010).

[39] R. E. Nelson, R. Vogt, and A. D. Frawley, Narrowing the uncertainty on the total charm cross section and its effect on the J/ψ cross section, Phys. Rev. C **87**, 014908 (2013).

[40] V. Cheung and R. Vogt, Polarized heavy quarkonium production in the color evaporation model, Phys. Rev. D **95**, 074021 (2017).

[41] V. Cheung and R. Vogt, Polarization of prompt J/ψ and Υ(1S) production in the color evaporation model, Phys. Rev. D **96**, 054014 (2017).

[42] V. Cheung and R. Vogt, Production and polarization of prompt J/ψ in the improved color evaporation model using the k_T-factorization approach, Phys. Rev. D **98**, 114029 (2018).

[43] V. Cheung and R. Vogt, Production and polarization of prompt $\upsilon(n\mathrm{S})$ in the improved color evaporation model using the k_T-factorization approach, Phys. Rev. D **99**, 034007 (2019).

[44] M. L. Mangano, P. Nason, and G. Ridolfi, Heavy quark correlations in hadron collisions at next-to-leading order, Nucl. Phys. B **373**, 295 (1992).

[45] M. L. Mangano, P. Nason, and G. Ridolfi, Fixed target hadroproduction of heavy quarks, Nucl. Phys. B **405**, 507 (1993).

[46] C. Y. Lo and J. D. Sullivan, Transverse momentum distributions in Drell-Yan processes, Phys. Lett. B **86**, 327 (1979).

[47] P. Nason, S. Dawson, and R. K. Ellis, The total cross-section for the production of heavy quarks in hadronic collisions, Nucl. Phys. B **303**, 607 (1988).

[48] K. J. Eskola, P. Paakkinen, H. Paukkunen, and C. A. Salgado, EPPS16: Nuclear parton distributions with LHC data, Eur. Phys. J. C **77**, 163 (2017).

[49] G. Onengut *et al.* (CHORUS Collaboration), Measurement of nucleon structure functions in neutrino scattering, Phys. Lett. B **632**, 65 (2006).

[50] J. Adam *et al.* (ALICE Collaboration), Centrality dependence of inclusive J/ψ production in $p-$Pb collisions at $\sqrt{s_{NN}} = 5.02$ TeV, J. High Energy Phys. 11 (2015) 127.

[51] T. Kitagaki *et al.* (E745 Collaboration), A new method to investigate the nuclear effect in leptonic interactions, Phys. Lett. B **214**, 281 (1988).

[52] V. Emel'yanov, A. Khodinov, S. R. Klein, and R. Vogt, The effect of shadowing on initial conditions, transverse energy and hard probes in ultrarelativistic heavy ion collisions, Phys. Rev. C **61**, 044904 (2000).

[53] R. Vogt, Are the J/ψ and $\chi_c A$ dependencies the same? Nucl. Phys. A **700**, 539 (2002).

[54] C. Lourenco, R. Vogt, and H. K. Woehri, Energy dependence of J/ψ absorption in proton-nucleus collisions, J. High Energy Phys. 02 (2009) 014.

[55] D. C. McGlinchey, A. D. Frawley, and R. Vogt, Impact parameter dependence of the nuclear modification of J/ψ production in $d+$Au collisions at $\sqrt{s_{NN}} = 200$ GeV, Phys. Rev. C **87**, 054910 (2013).

[56] R. L. Anderson *et al.*, Measurement of the *A* Dependence of J/ψ Photoproduction, Phys. Rev. Lett. **38**, 263 (1977).

[57] S. J. Brodsky, E. Chudakov, P. Hoyer, and J. M. Laget, Photoproduction of charm near threshold, Phys. Lett. B **498**, 23 (2001).

[58] B. Abelev *et al.* (ALICE Collaboration), Coherent J/ψ photoproduction in ultra-peripheral Pb-Pb collisions at $\sqrt{s_{NN}} = 2.76$ TeV, Phys. Lett. B **718**, 1273 (2013).

[59] E. Abbas *et al.* (ALICE Collaboration), Charmonium and e^+e^- pair photoproduction at mid-rapidity in ultra-peripheral Pb-Pb collisions at $\sqrt{s_{NN}} = 2.76$ TeV, Eur. Phys. J. C **73**, 2617 (2013).

[60] V. Khachatryan *et al.* (CMS Collaboration), Coherent J/ψ photoproduction in ultra-peripheral PbPb collisions at $\sqrt{s_{NN}} = 2.76$ TeV with the CMS experiment, Phys. Lett. B **772**, 489 (2017).

[61] A. Capella and E. G. Ferreiro, J/ψ suppression at $\sqrt{s} = 200$-GeV in the comovers interaction model, Eur. Phys. J. C **42**, 419 (2005).

[62] S. Gavin and R. Vogt, J/ψ suppression from hadron-nucleus to nucleus-nucleus collisions, Nucl. Phys. B **345**, 104 (1990).

[63] J. W. Cronin, H. J. Frisch, M. J. Shochet, J. P. Boymond, R. Mermod, P. A. Piroue, and R. L. Sumner, Production of hadrons with large transverse momentum at 200, 300, and 400 gev, Phys. Rev. D **11**, 3105 (1975).

[64] R. Vogt (Hard Probes Collaboration), The *A* dependence of open charm and bottom production, Int. J. Mod. Phys. E **12**, 211 (2003).

[65] X. N. Wang, Where is the Jet Quenching in Pb$+$Pb Collisions at 158*A* GeV? Phys. Rev. Lett. **81**, 2655 (1998).

[66] S. J. Brodsky, P. Hoyer, A. H. Mueller, and W.-K. Tang, New QCD production mechanisms for hard processes at large *x*, Nucl. Phys. B **369**, 519 (1992).

[67] T. Gutierrez and R. Vogt, Leading charm in hadron nucleus interactions in the intrinsic charm model, Nucl. Phys. B **539**, 189 (1999).

[68] B. W. Harris, J. Smith, and R. Vogt, Reanalysis of the EMC charm production data with extrinsic and intrinsic charmat NLO, Nucl. Phys. B **461**, 181 (1996).

[69] S. Paiva, M. Nielsen, F. S. Navarra, F. O. Duraes, and L. L. Barz, Virtual meson cloud of the nucleon and intrinsic strangeness and charm, Mod. Phys. Lett. A **13**, 2715 (1998).

[70] M. Neubert, Heavy quark symmetry, Phys. Rep. **245**, 259 (1994).

[71] F. M. Steffens, W. Melnitchouk, and A. W. Thomas, Charm in the nucleon, Eur. Phys. J. C **11**, 673 (1999).

[72] T. J. Hobbs, J. T. Londergan, and W. Melnitchouk, Phenomenology of nonperturbative charm in the nucleon, Phys. Rev. D **89**, 074008 (2014).

[73] J. Pumplin, H. L. Lai, and W. K. Tung, The charm parton content of the nucleon, Phys. Rev. D **75**, 054029 (2007).

[74] P. M. Nadolsky, H. L. Lai, J. Gao, J. Huston, J. Pumplin, C. Schmidt, D. Stump, and C. P. Yuan, Implications of CTEQ global analysis for collider observables, Phys. Rev. D **78**, 013004 (2008).

[75] S. Dulat, T. J. Hou, J. Gao, J. Huston, J. Pumplin, C. Schmidt, D. Stump, and C. P. Yuan, Intrinsic charm parton distribution functions from CTEQ-TEA global analysis, Phys. Rev. D **89**, 073004 (2014).

[76] P. Jimenez-Delgado, T. J. Hobbs, J. T. Londergan, and W. Melnitchouk, New Limits on Intrinsic Charm in the Nucleon From Global Analysis of Parton Distributions, Phys. Rev. Lett. **114**, 082002 (2015).

[77] R. D. Ball *et al.* (NNPDF Collaboration), A determination of the charm content of the proton, Eur. Phys. J. C **76**, 647 (2016).

[78] S. J. Brodsky, A. Kusina, F. Lyonnet, I. Schienbein, H. Spiesberger, and R. Vogt, A review of the intrinsic heavy quark content of the nucleon, Adv. High Energy Phys. **2015**, 341547 (2015).

[79] J. Blümlein, A kinematic condition on intrinsic charm, Phys. Lett. B **753**, 619 (2016).

[80] R. S. Sufian, T. Liu, A. Alexandru, S. J. Brodsky, G. F. de Téramond, H. G. Dosch, T. Draper, K. F. Liu, and Y. B. Yang, Constraints on charm-anticharm asymmetry in the nucleon from lattice QCD, Phys. Lett. B **808**, 135633 (2020).

[81] S. J. Brodsky, G. I. Lykasov, A. V. Lipatov, and J. Smiesko, Novel heavy-quark physics phenomena, Prog. Part. Nucl. Phys. **114**, 103802 (2020).

[82] R. Vogt, Heavy flavor azimuthal correlations in cold nuclear matter, Phys. Rev. C **98**, 034907 (2018).

[83] R. Vogt, $b\bar{b}$ kinematic correlations in cold nuclear matter, Phys. Rev. C **101**, 024910 (2020).

[84] M. B. Johnson, B. Z. Kopeliovich, I. K. Potashnikova, P. L. McGaughey, J. M. Moss, J. C. Peng *et al.*, Energy Loss of Fast Quarks in Nuclei, Phys. Rev. Lett. **86**, 4483 (2001).